Title

A mechanistic understanding of oxygen isotopic changes in the Western United States at the Last Glacial Maximum

Authors

Tabor, Clay

Lofverstrom, Marcus

Oster, Jessica

et al.

Publication Date

2021-12-01

DOI

10.1016/j.quascirev.2021.107255

Peer reviewed

A Mechanistic Understanding of Oxygen Isotopic Changes in the Western United States at the Last Glacial Maximum

Authors:
Clay Tabor[1*], Marcus Lofverstrom[2], Jessica Oster[3], Barbara Wortham[4], Cameron de Wet[3], Isabel Montañez[4], Alan Rhoades[5], Colin Zarzycki[6], Chengfei He[7], Zhengyu Liu[7]

Affiliations:
[1*]Department of Geosciences, University of Connecticut, Storrs, CT 06269, USA
[2]Department of Geosciences, University of Arizona, Tucson, AZ 85719, USA
[3]Department of Earth and Environmental Sciences, Vanderbilt University, Nashville, TN 37240, USA
[4]Department of Earth and Planetary Sciences, University of California–Davis, Davis, CA 95616, USA
[5]Climate and Ecosystem Sciences Division, Lawrence Berkeley National Laboratory, Berkeley, California 94720, USA
[6]Department of Meteorology and Atmospheric Science, Pennsylvania State University, University Park, Pennsylvania 16802, USA
[7]Department of Geography, Ohio State University, Columbus, Ohio 43210, USA

Corresponding Author:
[*]Clay Tabor (clay.tabor@uconn.edu)

Highlights:
- iCESM and forward proxy models used to understand $\delta^{18}O$ changes in western US at LGM
- North Pacific storms contribute to southward shift of moisture in western US at LGM
- Lower $\delta^{18}O$ of precipitation in western US at LGM due primarily to increased rainout
- Forward proxy model outputs generally agree with speleothem records
- Combination of climate and proxy models improve understanding of speleothem $\delta^{18}O$

Abstract:

At the Last Glacial Maximum (LGM), records suggest drier conditions in the northwest United States and wetter conditions in the southwest United States relative to present-day as well as widespread changes in the isotopic composition of water. However, the mechanisms responsible for these changes remain ambiguous. Here, we explore differences in western United States hydroclimate between the LGM and preindustrial with a water isotope tracer enabled Earth System Model. We then use proxy forward models to compare simulated and recorded $\delta^{18}O$ in speleothems. We find that the pattern of hydroclimate response in the western United States at the LGM relates to a combination of 1) increased frequency and southward shifted wintertime extratropical cyclones in the North Pacific, 2) greater rainout of moisture as it moves over the continent, and 3) reduced evaporation in the cooler LGM climate. The simulated lower $\delta^{18}O$ of precipitation at the LGM relates predominantly to the increase in winter precipitation efficiency, with a secondary contribution from relatively more winter precipitation in the Great Basin region. Both surface temperature and ice sheet extent contribute to these hydroclimate changes at the LGM. Comparisons between $\delta^{18}O$ from proxy forward models and speleothem records in the western United States show general agreement at the LGM, with increasing depletion moving

towards the continental interior. This study highlights the similarities and differences between hydrologic and $\delta^{18}O$ changes at the LGM and emphasizes the utility of model-proxy comparison for interpretation.

1. Introduction

The Western United States (W-US), defined here as states west of the Rocky Mountains, is home to over 66 million people, spans 1.88 million km^2, and produces almost 23% of the country's gross domestic product (US Census Bureau 2019 data; Bureau of Economic Analysis 2019 data). The geography and topography of the W-US encompasses a wide range of climates in a relatively confined region, with desert climate in the southwest, dry to wet Mediterranean climate along the Pacific coast, semi-arid steppe land extending into the continental interior, and a variety of alpine climates along the mountain ranges (Kottek et al., 2006). Seasonal-to-interdecadal synoptic patterns of ocean-atmosphere variability in the Pacific modulate W-US precipitation (e.g., Dettinger et al., 1998), which is largely a product of extratropical cyclones during the winter, particularly along the Pacific coast (Chang et al., 2015). Inhabitants of the W-US depend on this seasonal precipitation to replenish snowpack, groundwater, and surface reservoirs for the subsequent dry summer season.

Given the significance of the W-US to food production and economics, there has been a significant number of studies on how this region will respond to anthropogenic climate change (e.g., Hamlet and Lettenmaier, 2007; Dettinger et al., 2015; Rhoades et al., 2020a, b). Many simulations suggest increased risk of drought and seasonal precipitation variability in the coming decades to centuries as the climatic effects of greenhouse gas emissions become more pronounced (e.g., Seager et al., 2007; Diffenbaugh et al., 2015; Swain et al., 2018). However, there remains significant uncertainty in the degree of hydrologic change regionally with warming. Furthermore, the diversity of climates in the W-US will not respond uniformly to climate change due to the variety of dynamic drivers of hydroclimate in the region. Recent work suggests a similar pattern of hydroclimate change in the W-US under past and future forcing scenarios, which highlights the

value in exploring past climate to understand current and future climate change (Rehfeld et al., 2020).

Evidence for a spatially varied hydroclimate response in the W-US to climate change exists in proxy records of the Last Glacial Maximum (LGM, ca. 21,000 years before present; e.g., Oster et al., 2015a; 2020; Feakins et al., 2019; Hudson et al., 2019). During this time, climate reconstructions of the W-US suggest comparatively wetter conditions in the south and drier conditions in the north. Of the many proxy archives gathered in the W-US, measurements of $\delta^{18}O$ in cave records, known as speleothems, have proven to be particularly valuable because they can produce long, continuous records of past hydroclimate change with robust age constraints (e.g., Oster and Kelley, 2016). However, the various mechanisms that produced these $\delta^{18}O$ signals are difficult to deconvolve and continue to be debated.

Climate model simulations have long explored this unique dipole response to understand W-US climate dynamics (e.g., Manabe and Broccoli, 1985; COHMAP Members, 1998; Oster et al., 2015a; Lofverstrom and Liakka, 2016; Lora et al., 2017; Lora et al., 2018; Morrill et al., 2018; Lofverstrom, 2020). Although many climate models configured with period appropriate boundary conditions can capture the measured pattern of hydrologic change in the W-US at the LGM (e.g., Kageyama et al. 2021), debate remains as to the underlying dynamics responsible for the spatial pattern of wet and dry. A long-standing hypothesis suggests that southward-displaced westerlies lead to shift in W-US moisture at the LGM (e.g., COHMAP Members, 1988). More recently, alternative hypotheses attribute altered LGM moisture to a strengthening and meridional compression of the storm track (Oster et al., 2015a) or a primarily thermodynamic control arising from steepened temperature and moisture gradients from the Pacific inland due to the cooling influence of the Laurentide Ice Sheet (Boos, 2012; Lofverstrom and Liakka, 2016; Morrill et al.,

2018). Other hypotheses call upon a strengthening of moisture transport to W-US from a southwesterly, subtropical source (Lyle et al., 2012) perhaps due to increased contributions from atmospheric rivers (Lora et al., 2017, Lofverstrom, 2020) driven by a southward shift of the ITCZ and intensification of North Pacific Hadley circulation (McGee et al., 2018).

Debate also surrounds model-proxy comparison. Although the general pattern of W-US hydroclimate response at the LGM is robust, proxy records are not direct measures of hydroclimate, which can make model-proxy comparison difficult. For example, proxy-data archives that record amount weighted $\delta^{18}O$ values of precipitation ($\delta^{18}O_p$) may be influenced by regional differences in $\delta^{18}O$ values from different moisture sources, the relative amount of precipitation from different moisture sources, rainout and infiltration of water vapor during transport, seasonality of precipitation, precipitation efficiency, and local below cloud processes (e.g., Pausata et al., 2011; Pausata and Lofverstrom, 2015; Tabor et al., 2018; He et al., 2021). In the case of $\delta^{18}O$ values of the speleothem carbonate ($\delta^{18}O_c$), changes in cave air temperature at the time of deposition, mixing of water sources, and evaporation in the soil and karst compound the complexity (e.g., Fairchild et al. 2006; Tremaine et al., 2011; Baker et al., 2012). Therefore, attribution of $\delta^{18}O$ variations to changes in temperature or precipitation is often overly simplified and potentially erroneous. Water isotopologue tracking enabled Earth system models have the potential to separate the various climate signals stored in isotopic records. By tracking the physical and dynamical movement of $H_2{}^{18}O$ and $H_2{}^{16}O$ within the Earth system, one can better determine what mechanisms and interactions are responsible for the $\delta^{18}O$ signals found in W-US at the LGM.

Studies typically utilize monthly climatologies of model outputs when informing proxy interpretations. However, exclusively exploring climatology can limit understanding about the specific weather patterns underlying past climate signals. For example, atmospheric rivers (ARs)

are elongated plumes of concentrated water vapor that overall account for roughly 90% of the total meridional water vapor flux in the mid latitudes but individually only last for hours to days (Zhu and Newell, 1998; Guan and Waliser, 2015). Recent work by Lora et al. (2017) and Lofverstrom (2020) suggests that atmospheric rivers are largely responsible for the moisture increase in the southwest US at the LGM. Yet most studies are unable to distinguish the role of ARs in W-US moisture budget due to working with monthly means, which cannot well separate the drivers of past hydroclimate change. Therefore, high temporal frequency outputs from models are required to better understand the mechanisms driving the proxy signals in the W-US at the LGM.

Here, we present preindustrial (PI) and LGM Earth system model simulations that include online water isotopologue tracers. Our experiments include high temporal frequency data outputs. Together, these features allow for new insights into the drivers of W-US hydroclimate and isotopic change at the LGM. We subsequently use proxy forward models to compare our climate modeling results to speleothem $\delta^{18}O$ records from the W-US. In section 2, we detail the earth system model, experiment configurations, and water tracking techniques that we use to determine mechanisms responsible for W-US hydroclimate and isotopic change at the LGM. In section 3, we present our results, including W-US changes between LGM and PI in climatology and dynamics as well as several sensitivity experiments with different combinations of LGM and PI boundary conditions. In section 4, we follow with a comparison between model simulations and speleothem $\delta^{18}O$ records, made possible using two karst system proxy models. Finally, we summarize our findings in section 5.

2. Methods

2.1 Earth System Model Approach

Here, we use the Community Earth System Model version 1.3 with water isotopologue tracking of oxygen and hydrogen in the atmosphere, land, ocean, sea ice, and runoff components (iCESM1.3; Nusbaumer et al., 2017; He et al., 2021). The climate of CESM1.3 is broadly similar to CESM1.2, which captures the observed PI and historical mean state and variability to a high accuracy (Hurrell et al., 2013); the simulated present-day water isotopologues are also similar in both model versions (Brady et al. 2019). Moreover, iCESM1.3 demonstrates skill capturing the observed spatial pattern of $\delta^{18}O_p$ depletion moving inland from the US west coast (Figure S1) and more generally when compared with proxy records from the LGM (e.g., Zhu et al., 2017; Tierney et al., 2020; He et al., 2021). CESM1 has also been used in paleotempestology research (Skinner et al., 2020; Shields et al., 2021).

This study explores changes in W-US hydroclimate between the Last Glacial Maximum (LGM; 21 ka) and preindustrial (PI; 1850 CE). To this end, we use four configurations of iCESM1.3 to simulate the two time periods of interest (Figure S2). Our LGM boundary conditions follow the Paleoclimate Modelling Intercomparison Protocol version 4 (PMIP4) for the LGM (Kageyama et al., 2017), including ICE-6G ice sheet reconstructions (Peltier et al., 2015), 21 ka orbital configuration (Laskar et al., 2010), and 190 ppm CO_2 (Bereiter et al., 2015). Initial isotopic distribution in the ocean comes from the GISS interpolated ocean $\delta^{18}O$ dataset (LeGrande and Schmidt, 2006) with global enrichment of +1.05‰ in the LGM simulation to account for the increase in terrestrial ice (Duplessy et al., 2002). In addition to the full LGM forcing simulation, we perform two sensitivity tests. One sensitivity experiment, PI_Topo, uses all LGM boundary conditions except topography, which is set to PI values. In other words, the PI_Topo experiment includes LGM greenhouse gases, orbit, ocean conditions, land surface types, and land/sea mask with PI ice sheet elevation. The other sensitivity experiment, LGM_Topo, uses all PI boundary

conditions except topography, which is set to LGM values. In other words, the LGM_Topo experiment includes PI greenhouse gases, orbit, ocean conditions, land surface types, and land/sea mask with LGM ice sheet elevation.

We initialize and spin-up the water isotopologues in the LGM and PI experiments using the fully coupled configuration of iCESM1.3 with 1.9°×2.5° horizontal resolution atmosphere (Community Atmosphere Model 5; CAM5) and land (Community Land Model 4; CLM4) components, and nominal 1° horizontal resolution ocean (Parallel Ocean Program 2; POP2) and sea ice (Community Sea Ice Model 4; CICE4) components. We integrated these fully coupled simulations until the climates and distributions of water isotopologues are near equilibrium (long-term drift is small compared to interannual variability). We then switch to a 0.9°×1.25° horizontal resolution configuration of iCESM1.3 with dynamically evolving atmosphere and land models (CAM5/CLM4 only simulation) but prescribed monthly varying sea-surface conditions (temperature, sea-ice extent, and $\delta^{18}O$) from the last 50 years of the fully coupled simulations as input. The increased horizontal resolution allows the model to better resolve the topography that influences the climate in Western North America. To spin-up the land model (notably, soil temperatures and hydrology) at higher resolution, we first interpolate data from the 1.9°×2.5° resolution simulations to the 0.9°×1.25° grid, then run the CAM5/CLM4 only simulations for 50 years using an annual cycle of SSTs from the mean of the final 50 years of the fully coupled simulations. Next, we extend the CAM5/CLM4-only simulations for an additional 50 years with time varying SSTs from the final 50 years of the fully coupled simulations. All analyses presented here are based on the final 45 years of the simulations (the first 5 years are discarded as model spin up). Below we discuss results from the W-US (land area south of the LGM Laurentide Ice Sheet (LGM LIS) edge between 29°N-49°N and 110°W-125°W). Further, we divide the W-US into the

Southwest United States (SW-US; land area between 29°N-39°N and 110°W-125°W) and the Northwest United States (NW-US; land area between 39°N-49°N and 110°W-125°W; see white dashed lines in Figure 1). This W-US region is considered for the bulk of our model analyses (Sections 3.1-3.5). However, we discuss locations further east in Sections 3.6, 4.2, and 4.3 due to a limited number of W-US speleothem records that cover the late glacial period.

We employ several analysis techniques to interpret hydrologic change in the W-US at the LGM. To better understand the sources and isotopic composition of moisture reaching the W-US, we utilize the water "tagging" feature within iCESM1.3, which tracks water and its isotopic composition from evaporation to deposition in user defined regions. Here, we focus on regions within the North Pacific, as this area is the source of most moisture transported to the W-US. This unique feature of iCESM1.3 has been previously utilized to understand paleoclimate variations in $\delta^{18}O_p$ (e.g., Tabor et al., 2018; He et al., 2021). We also use the TempestExtremes feature detection algorithm (Ullrich and Zarzycki, 2017; Ullrich et al., 2021) to track two specific weather event types that largely drive the climatological changes in W-US hydrology. We output 6-hourly (instantaneous) variables of integrated vapor transport, sea level pressure, surface winds, and 500 and 300 hPa geopotential height to track atmospheric rivers (ARs) and extratropical cyclones (ETCs) in the North Pacific. Previous studies using versions of CESM in combination with TempestExtremes show skill simulating and tracking ARs and ETCs when compared with observations (e.g., Zarzycki, 2018; Rhoades et al., 2020a; 2020b).

Parameters for AR identification include: 1) a minimum integrated vapor transport (IVT) threshold of 250 kg/m/s; 2) a minimum Laplacian of IVT of 50,000 kg/m/s/degrees^2; 3) a minimum IVT area of 5 grid cells; 4) a radius of the discrete Laplacian of 20 grid cells; and 5) a minimum latitude of 15°N. These parameters create a similar pattern of North Pacific AR track density to

previous work (Rhoades et al., 2020a). ETCs are tracked by following local minima in the 6-hourly sea level pressure field. These minima must be at least 3 hPa lower than the background sea level pressure and storms with a positive geopotential thickness anomaly of at least 10 m between 300 and 500 hPa are excluded as warm core (i.e., tropical) cyclones. ETCs must last at least 60 hours and travel at least 10 degrees great circle distance such that stationary, climatological lows are not included. ETC counts from our iCESM1.3 PI simulation compare well with ETC counts produced using National Centers for Environmental Prediction Climate Forecast System Reanalysis data (Ullrich and Zarzycki, 2017).

2.2 Model-Proxy Comparison

2.2.1 Western U.S. speleothem $\delta^{18}O$ records drip water estimates

We compile W-US speleothem $\delta^{18}O$ records from the literature, including those from the SISALv2 database (Oster et al., 2019; Comas-Bru et al., 2020) and other records that have been published following the most recent SISAL update (Oster et al., 2020; Figure 2a). Three speleothem records from the W-US cover the LGM (21 ka): Cave of the Bells, Arizona (COB; Wagner et al., 2010), Fort Stanton Cave, New Mexico (FS; Asmerom et al., 2010), and Lake Shasta Caverns, California (LSC; Oster et al., 2020). An additional three speleothem records cover the late glacial period and are dated to within 2000 years of 21 ka: McLean's Cave, California (ML, maximum age ~19.4 ka; Oster et al., 2015b), Pinnacle Cave, Nevada of the Leviathan Chronology (LV, maximum age ~20 ka; Lachniet et al., 2014), and Cave Without a Name, Texas (CWN, maximum age ~19.3 ka; Feng et al., 2014). Of the speleothem records available for the W-US, only the Leviathan Chronology covers both the late glacial and the present. This lack of consistent coverage precludes us from computing anomalies in the speleothem $\delta^{18}O$ records to compare with

modeled LGM-PI $\delta^{18}O_p$ anomalies. Instead, our approach focuses on estimating the absolute values of LGM drip water following the guidelines for model-proxy comparison using speleothem records described in Comas-Bru et al. (2019). We complement this approach by also evaluating proxy forward modeling techniques to estimate drip water and calcite $\delta^{18}O$ using our climate model output (described below).

Following Comas-Bru et al., (2019), we compute the mean and standard deviations for the three records covering the interval 21 ka +/- 500 years. For the three records that cover the late glacial but not 21 ka (ML, LV, CWN), we calculated the mean and standard deviation of the oldest 500 years of each record. We then compute the estimated "LGM" drip water $\delta^{18}O$ for each cave location using these mean speleothem $\delta^{18}O$ values and the mean annual surface temperature from the LGM model output of the model gridbox nearest to each cave's location. We use two different calcite-water oxygen isotope-fractionation relationships in our calculations: the experimentally determined low-temperature equilibrium fractionation relationship of Kim and O'Neil (1997) and the empirically determined, cave-specific water-calcite oxygen isotope fractionation relationship of Tremaine et al. (2011). We compare these estimated LGM drip water values to the amount-weighted $\delta^{18}O_p$ taken from the iCESM1.3 experiments' mean annual and wettest consecutive three-month period for each cave location (Table S1).

2.2.2 Drip water forward modeling

To better understand the comparison between the iCESM1.3 experiments and the stalagmite records, we simulate stalagmite $\delta^{18}O$ values using two different forward modeling approaches that have been developed for cave environments: CaveCalc and Karstolution. In this and following sections, we will distinguish between the iCESM1.3 experiments as described above

in section 2.1 and the forward model experiments by referring to them as "CaveCalc runs" and "Karstolution runs," respectively. The first proxy system model, CaveCalc (Owen et al. 2018) forward models the evolution of carbonate fluid chemistry as water moves downward through the soil zone, the epikarst, and eventually into the cave. For CaveCalc, we input climatological (45-year mean) annual temperature and $\delta^{18}O_p$ from the PI and LGM iCESM1.3 experiments for the grid cells in which each of our cave sites are located. For simplicity, we leave all other input parameters as their default values following Owen et al. (2018), including a cave air pCO_2 of 1000 ppm. CaveCalc does not allow for the diffusional exchange of soil gas with the atmosphere, so we do not account for differences in atmospheric pCO_2 in these simulations. We run CaveCalc using the default multi_step_degassing Degassing/Precipitation Mode, which is meant to represent CO_2 degassing and calcite precipitation during speleothem growth, and the default value of 0.5 as the fraction of CO_2 removal per reaction step. During the model simulation, water undergoes progressive CO_2 degassing and precipitates calcite (maintaining a saturation of 1.0) until the solution reaches equilibrium with the cave air. We consider the mean $\delta^{18}O$ value of calcite precipitated over all the degassing steps as representative of the mean speleothem $\delta^{18}O$ formed during the LGM and PI at each cave site.

In contrast to CaveCalc, which produces one value for the estimated speleothem $\delta^{18}O$ for each of the LGM and PI time slices, Karstolution (Treble et al., in review) uses a time series as an input and outputs a modeled time series of calcite $\delta^{18}O$ that represent five different pseudo-stalagmites grown under conditions set by the user. Karstolution is a combination of KarstFor (Bradley et al., 2010; Baker and Bradley, 2010; Treble et al., 2013; Baker et al., 2014), which is a karst processes model, and ISOLUTION (Deininger et al., 2012), which is an isotope enabled fractionation model. Rather than the mean annual values of temperature and $\delta^{18}O_p$ used for

CaveCalc, Karstolution uses as input monthly time series of precipitation and evaporation amounts, temperature, and $\delta^{18}O_p$ from the iCESM1.3 experiments. In addition, the model uses a configuration file, which prescribes the fluxes through the karst portion of the model, the cave-air pCO_2, the cave-air temperature, and the relative humidity. Coupling of KarstFor and ISOLUTION to develop Karstolution allows for a better understanding of the impacts of climatic karst processes and in-cave effects on calcite $\delta^{18}O$, as the model can be tuned based on information from cave monitoring to represent the karst processes understood for a given cave system.

To run Karstolution, we use 45 years of monthly outputs, as opposed to the mean annual values used in CaveCalc, from the PI and LGM iCESM1.3 experiments from the grid cells that include each cave location. In these initial runs of Karstolution, cave-air pCO_2 was set to the atmospheric pCO_2 used for the iCESM1.3 experiments (190 ppm at LGM, 284.7 ppm at PI). The initial $\delta^{18}O$ value of the karst storage water and cave-air temperature in the configuration file was set to the mean annual $\delta^{18}O_p$ and temperature from the iCESM1.3 outputs for the cave location. The five hypothetical calcite $\delta^{18}O$ time series produced by Karstolution capture different configurations of mixing between reservoirs of water in the karst and soil water (Treble et al., in review). In this paper, we present the Karstolution results for Stalagmites 2 and 4 as these two simulated stalagmite time-series represent a short water-residence time end-member (Stalagmite 2) and a longer water-residence time end-member (Stalagmite 4) (Figure S3).

We completed a set of Karstolution runs for each cave location using the same settings at each site. However, to further explore the influence of in-cave processes on the forward-model results, we made use of extensive cave monitoring data that have been published for the two California Cave sites, LSC and ML, allowing us to compare the iCESM1.3 output with pseudo-stalagmites tuned with site-specific information. The relevant monitoring data that exist for these

sites include seasonal measurements of cave air *p*CO2 and relative humidity at LSC (Oster et al., 2020) and Black Chasm Cave, which is close to ML (Oster et al., 2012). A second set of Karstolution runs were carried out for these two sites using cave monitoring data and site-specific parameterization of cave seasonality and are referred to as "optimized" Karstolution runs. Based on these monitoring data, for ML we prescribed a cave-air pCO_2 of 1000 ppm for the year except for the Boreal summer (JJA), which was prescribed at 3000 ppm. The relative humidity was set at 95% and the cave-air temperature was set to the mean annual from the iCESM1.3 experiments. For ML, the temperature used is -2.2 °C with a 4 °C temperature increase for JJA. For LSC, we prescribed a cave-air pCO_2 of 470 ppm. The relative humidity was set to 89% for JJA and 95% for the rest of the seasons. The cave-air temperature was set to the mean annual from the iCESM1.3 experiments for the LSC location (2.3°C) with a 5 °C temperature increase for JJA.

3. Results

3.1 Climatology

As a spatial average, mean annual $\delta^{18}O_p$ decreases by 1.33‰ in the W-US at the LGM compared to PI, with the greatest reduction in the north-central to north-east portion of the study area, and minimal change along the west coast (Figure 1; Figure S4). Similarly, the SW-US and NW-US regions show reductions in mean annual $\delta^{18}O_p$ at the LGM of 0.79‰ and 1.70‰, respectively. There exist some similarities in the spatial patterns of changes in mean annual surface temperature, precipitation, and $\delta^{18}O_p$, in the W-US at the LGM. For example, regions of lower $\delta^{18}O_p$ are generally associated with areas of drying and enhanced surface cooling. However, these spatial relationships are the product of several changes in LGM climate, and local temperature and precipitation cannot be considered causative of the $\delta^{18}O_p$ response.

Figure 1: Annual differences in climate between LGM and PI for A) $\delta^{18}O_p$ of precipitation, B) precipitation and near surface winds, C) surface temperature, and D) precipitation minus evaporation. Northwest and Southwest United States regions outlined with dashed white lines. LGM continental configuration outlined in black.

Like the spatial pattern of precipitation observed in previous modeling and proxy data studies (e.g., COHMAP Members, 1988; Bartlein et al., 2011; Oster et al., 2015a; Morrill et al., 2018), the SW-US experiences a small mean annual increase in precipitation of 0.03 mm/day, while the NW-US experiences a pronounced mean annual decrease in precipitation of 0.47 mm/day (Figure 1; Figure S4). A decrease in evaporation associated with cooler surface temperatures further moistens the SW-US and results in a variable net moisture response in the NW-US despite the pervasive reduction in precipitation.

Because this study focuses on the mechanisms driving W-US changes in $\delta^{18}O_p$ at the LGM, precipitation amount is a primary interest. In the W-US, 58% and 61% of mean annual precipitation falls in winter (here defined as November to March) in the LGM and PI simulations, respectively (Figure S5), due primarily to extratropical cyclones. Although the winter contribution to mean annual precipitation decreases moving inland, much of the remaining W-US precipitation occurs during the fall and early spring and is also due primarily to extratropical cyclones. Winter hydroclimate, therefore, well reflects the mechanisms driving the annual $\delta^{18}O_p$ response in this region and will be the focus of the following results. Note, we do not limit our analyses to winter

precipitation when comparing with speleothem $\delta^{18}O$ in Section 3.6.

Figure 2: W-US speleothem records with near LGM data. A) Map and B) time series of W-US speleothem $\delta^{18}O$ records included in this study. Gray shading on B shows intervals of each record that are considered for the LGM comparisons with iCESM1.3. For records that extend to 21 ka, this includes 21 ka +/- 500 years. For records that do not extend to 21 ka, this includes the oldest 500 years of each record.

Figure 3: Winter (Nov-Feb) differences in climate between LGM and PI for A) $\delta^{18}O_p$ of precipitation, B) precipitation and near surface winds, C) surface temperature, and D) precipitation minus evaporation. Northwest and Southwest United States regions outlined with dashed white lines. LGM continental configuration outlined in black.

As expected, the W-US mean annual $\delta^{18}O_p$ response generally reflects the W-US winter $\delta^{18}O_p$ response between LGM and PI, especially along the North American west coast where the winter contribution to annual precipitation is greatest (Figure 3; Figure S6). Only more positive winter $\delta^{18}O_p$ in the south-central sector of the study region disagrees in sign with the mean annual response (see further discussion below). During winter, there is anomalous low-level onshore flow in the SW-US and offshore flow in the NW-US, which generally aligns with areas of more and less winter and annual precipitation. The winter surface temperature anomaly also agrees with the mean annual response, depicting rapid cooling towards the continental interior. Notably, the spatial

pattern of W-US winter $\delta^{18}O_p$ response at the LGM does not correlate with changes in temperature or precipitation amount.

3.2 Water Tagging

To better understand the simulated LGM $\delta^{18}O_p$ response, we track moisture that sources from different regions of the North Pacific. The results show that changes in both the winter $\delta^{18}O_p$ and precipitation in the Central East North Pacific region (CENP; here defined as the region 20°N-45°N, 180°W-US coast) contribute most significantly to the LGM $\delta^{18}O_p$ response in the W-US (Figure 4; Figure S7). First, $\delta^{18}O_p$ and $\delta^{18}O$ of water vapor ($\delta^{18}O_{wv}$) from the CENP region are relatively lower at the LGM than the PI. The similarity of $\delta^{18}O_p$ and $\delta^{18}O_{wv}$ changes from the CENP region signify that the W-US reduction in $\delta^{18}O_p$ at the LGM is largely a result of differences in the isotopic composition of the water vapor. The reduction of $\delta^{18}O_{wv}$ is small in the eastern North Pacific, which indicates evaporative conditions, likely related to cooling, offset the ~1‰ higher mean ocean $\delta^{18}O$ at the LGM. The reduction of $\delta^{18}O_{wv}$ increases substantially moving inland, suggesting that rainout drives the lowering of $\delta^{18}O$ from the CENP region in the continental interior. Moreover, the similar responses of $\delta^{18}O_{wv}$ and $\delta^{18}O_p$ in the W-US from the CENP region suggest little difference in fractionation during condensation between the LGM and PI, ruling out a significant role for fractionation in the $\delta^{18}O_p$ response. In fact, there is a slightly larger difference in $\delta^{18}O$ values between vapor and precipitation at the LGM relative to PI (not shown), possibly related to cooler temperatures that increase fractionation during condensation. Second, in addition to producing about half of the total winter precipitation in the W-US, the CENP region contributes relatively more of the total precipitation to the W-US during the LGM than during the PI at the expense of precipitation sourced from farther west and north as well as reduced recycling over

Figure 4: Winter (Nov-Mar) differences in climate from the Central North Pacific region between LGM and PI for A) $\delta^{18}O_p$ of precipitation, B) $\delta^{18}O_{wv}$ of water vapor, C) percentage change in contribution to total precipitable water, and D) percentage change in contribution to total precipitation. Northwest and Southwest United States regions and Central North Pacific tagged region outlined with dashed white lines. LGM continental configuration outlined in black.

land. Reduction in precipitation from these more distant sources that provide relatively depleted moisture to the W-US limits the overall depletion in $\delta^{18}O_p$ at the LGM, particularly along the west coast. However, the 5-10% increase in W-US precipitation from the CENP region means the lower $\delta^{18}O_p$ from this region has greater weight in the mean annual $\delta^{18}O_p$ decrease at the LGM. The relative increase in W-US precipitation from the CENP region at the LGM mirrors an increase in W-US precipitable water from the CENP region, suggesting that changes in moisture transport from the CENP region plays an important role in winter precipitation response.

3.3 Tempestology

We further explore the changes in moisture transport by tracking simulated winter extratropical cyclones (ETCs) and atmospheric rivers (ARs). The relative increase in winter CENP moisture reflects an increase and southward shift in North Pacific ETC activity during the LGM (Figure 5; Figure S8). Greater winter cyclogenesis in the North Pacific appears related to locations of increased baroclinicity associated with stronger latitudinal temperature gradients (Kageyama et al., 2016; Routson et al., 2019); LGM topography also likely plays a role (see further discussion in section 3.5). Despite a general increase in ETC activity in the Northeast Pacific between 25°-55°N, there is a decrease in total moisture transport in this region. However, moisture transport remains unexpectedly high relative to the decrease in precipitable water near the southwest coast, likely due to an intensification and southward shift of the low-level jet associated with greater ETC activity (Laîné et al., 2009; Wang et al., 2018). Likewise, AR frequency near the southwest coast shows only a small reduction at the LGM relative to PI. The winter AR response at the LGM likely relates to the winter ETC response as ARs are almost always associated with ETCs (Guo et al., 2020). Note, our use of AR thresholds chosen for present-day societal impacts might be partly responsible for the discrepancy in response between ETCs and ARs. Given the dramatic cooling and overall decrease in precipitable water at the LGM, the similar amount of winter moisture transport into the SW-US between time periods is noteworthy. However, there is an increase in precipitation throughout the SW-US region at the LGM, suggesting that maintenance of Pacific winter moisture transport is not the only mechanism driving the SW-US hydroclimate response. In the NW-US, cooler temperatures, and associated reduction in humidity, in combination with a weaker low-level jet lead to a large decrease in moisture transport. In addition, the southward shift

in the location of winter ETCs near the west coast at the LGM modifies the location of offshore and onshore flow such that the warm sector impacts further south. Together, these changes help to reduce precipitation in the NW-US.

Figure 5: Winter (Nov-Mar) differences in storm activity between LGM and PI for A) total number of marine forming extratropical cyclones over 45 years of simulation using 6 hourly data and a 6° search radius, B) total number of atmospheric rivers over 45 years of simulation using 6 hourly identifications, C) integrated vapor transport, and D) 850 hPa winds. Northwest and Southwest United States regions outlined with dashed white lines. LGM continental configuration outlined in black.

Figure 6: Winter (Nov-Mar) differences in climate between LGM and PI as a vertical cross section from 35°-40°N for A) $\delta^{18}O_{wv}$ of water vapor, B) LGM and PI lines of constant potential temperature, C) cloud fraction, and D) specific humidity. LGM topography is shaded gray.

3.4 Efficiency and Seasonality

The $\delta^{18}O_p$ and precipitation responses in the W-US at the LGM are also due to greater precipitation efficiency, defined here as the amount of precipitation in a region relative to the

amount of column integrated water vapor in the same region. Enhanced land-sea temperature contrast at the LGM results in steeper density gradients, a rapid reduction in saturation humidity, and greater condensation moving inland (Figure 6; Figure 3; Figure S9), which produce more moisture convergence and precipitation as the winter storm systems move inland despite reduced total precipitable water. Enhanced storminess and more upslope flow along topography on the west coast of the US may also contribute to the greater winter precipitation efficiency at the LGM. Higher coastal $\delta^{18}O_{wv}$, which results from increased moisture flux from the nearby ocean and the increase in mean seawater $\delta^{18}O$ at the LGM, quickly transitions to lower $\delta^{18}O_{wv}$ farther inland because of increased rainout from stronger uplift and cooling along constant density surfaces. This enhanced rainout is largely responsible for the winter reduction in $\delta^{18}O_{wv}$ and $\delta^{18}O_p$ as moisture is transported into the continental interior at the LGM. Even with greater precipitation efficiency, NW-US precipitation is reduced due to the large decrease in total moisture transport. The cold, dry air flowing down the LGM LIS furthermore suppresses precipitation along the southern ice edge.

Because $\delta^{18}O_p$ is a weighted quantity, changes in precipitation seasonality can contribute to $\delta^{18}O_p$. Winter $\delta^{18}O_p$ is generally lower than other seasons in both the LGM and PI simulations (Figure 7). The SW most portion of the W-US is an exception to this in the LGM simulation. Here, there is an increase in $\delta^{18}O_p$ during the winter relative to summer due to more near coastal moisture in the cold season. Because of the generally lower $\delta^{18}O_p$ in the winter, more precipitation in the winter relative to the summer drives the mean annual $\delta^{18}O_p$ signal towards lower values in the W-US. Indeed, winter precipitation increases relative to summer precipitation in much of the W-US at the LGM. This seasonal shift is both a result of increased winter precipitation associated with greater ETC activity and precipitation efficiency, and decreased spring/summer precipitation associated with reduced convection in the LGM climate, possibly due to entrainment of cool, dry

air from further north (Bhattacharya et al., 2017). The increase in winter precipitation at the LGM is most pronounced around the Great Basin, where winter precipitation increases by ~15% with a clear response in mean annual $\delta^{18}O_p$. Outside of this region, however, seasonal changes in precipitation increase $\delta^{18}O_p$ at the LGM. In most of the W-US, areas of higher $\delta^{18}O_p$ caused by changes in precipitation seasonality are offset by lower isotopic values of precipitation, which are largely a result of increased precipitation efficiency at the LGM.

Figure 7: Differences in seasonality for A) LGM $\delta^{18}O_p$ of precipitation between winter (Nov-Mar) and annual, B) changes in percent contribution of winter precipitation to annual precipitation between LGM and PI, C) the impact of LGM precipitation seasonality on PI $\delta^{18}O_p$ (i.e. comparing $\delta^{18}O_p$ calculated using LGM precipitation and PI $\delta^{18}O$ against $\delta^{18}O_p$ calculated using PI precipitation and PI $\delta^{18}O$), and D) changes in winter (Nov-Mar) precipitation rate relative to total precipitable water between LGM and PI. Northwest and Southwest United States regions outlined with dashed white lines. LGM continental configuration outlined in black.

3.5 Sensitivity Experiments

Sensitivity experiments using either PI boundary conditions with LGM topography (LGM_Topo) or LGM boundary conditions with PI topography (PI_Topo; see Section 2.1 for additional details) show that the W-US responses at the LGM are not the result of a single forcing. Neither sensitivity simulation produces as much mean annual reduction in $\delta^{18}O_p$ in the W-US as the full forcing LGM simulation (Figure 8), suggesting contributions from both dynamic and thermodynamic processes. That said, the large-scale North Pacific circulation anomaly at the LGM results primarily from SST and albedo responses as seen in LGM_topo while the west coast precipitation increase results primarily from topographic changes as seen in PI_Topo. The overall SW-US precipitation response at the LGM appears to be a combination of LGM_Topo and PI_Topo forcings. In contrast, the general reduction in precipitation found in the NW-US region at the LGM is not a clear combination of topographic and SST changes. The lack of topographic barrier and dry downslope flow from the high pressure over the North American ice sheets allows for more onshore flow in PI_Topo, resulting in an increase in winter precipitation. Likewise, there is an increase in NW-US coastal precipitation in LGM_Topo related to the increase in storm frequency (Figure 9); however, outflow from the North American ice sheets dampens this response at the northern edge of the NW-US. In the full forcing LGM experiment, flow off the ice sheets in combination with cooler surface temperatures suppress the mechanisms driving increased NW-US coastal precipitation in PI_topo and LGM_topo. Even though both sensitivity experiments show increased and shifted winter ETC activity in the North Pacific, only the LGM_Topo experiment results in an associated increase in moisture transport by ARs, suggesting that the cooling at the LGM is primarily responsible for limiting the amount of moisture and precipitation in the W-US. There is also a large difference in the strength of the North Pacific low-level jet between simulations, with a pronounced southward shift in LGM_topo. This dramatic change in jet strength

clearly plays a role in vapor transport into the W-US, but the exact mechanisms for this response

Figure 8: Differences between sensitivity tests and PI. Differences in annual $\delta^{18}O_p$ of precipitation between A) LGM_Topo and PI and B) PI_Topo and PI; winter (Nov-Mar) precipitation and near surface winds between C) LGM_Topo and PI and D) PI_Topo and PI; winter precipitation rate relative to total precipitable water between I) LGM_Topo and PI and J) PI_Topo and PI

are beyond the scope of this study. These sensitivity experiments also confirm that intensified land-ocean temperature gradients enhance winter precipitation efficiency in the W-US at the LGM as the PI_Topo experiment shows an increase in coastal precipitation efficiency. There is also enhanced precipitation efficiency in the W-US in the LGM_Topo experiment because of increased storm frequency and surface cooling on land due to the inclusion of LGM topography. Like in the full forcing LGM experiment, enhanced rainout of moisture moving inland leads to depletion of $\delta^{18}O_p$ in these idealized cases, quickly offsetting potential enrichment due to increased moisture from nearby sources and mean ocean $\delta^{18}O$ at the LGM. However, interpretations from our idealized simulations are somewhat limited due to the lack of dynamic ocean and sea ice, which may prevent realization of the full effects of these changes on the climate system.

3.6 Proxy Model Comparison

A comparison of estimated LGM drip water $\delta^{18}O$ values with modeled mean annual and wet season mean LGM $\delta^{18}O_p$ is presented in Figure 10 a. Here, we define wet season precipitation as the three consecutive months that contribute most to annual rainfall at a particular location and time (see Table S1). Thus, the wet season differs from site to site in this comparison. Estimated drip water $\delta^{18}O$ values calculated using the Tremaine et al. (2011) empirical temperature-fractionation relationship are ~0.5 to 1‰ lower than values calculated using the Kim and O'Neil (1997) fractionation relationship. For many of the sites, one or both drip water estimates are within 0.5‰ of the modeled $\delta^{18}O_p$. At our most western sites, LSC and ML, drip water estimated using the Kim and O'Neil relationship is more closely aligned with modeled $\delta^{18}O_p$, which is similar between the mean annual and wet season (DJF at these sites). At LV, both fractionation relationships produce estimated drip water that is within 0.5‰ of the mean annual $\delta^{18}O_p$ from the

model, while the wet season (DJF) $\delta^{18}O_p$ value is almost 2‰ more negative than the estimated LGM drip water values. At FS, the Tremaine et al. (2011) fractionation relationship produces an estimated drip water value that is within ~1‰ of the model mean annual $\delta^{18}O_p$ value, whereas the wet season (JJA) mean is much more negative than the estimated drip water. At COB, the Kim and O'Neil (1997) relationship produces estimated drip water that is very close (within ~0.5‰) of the modeled mean annual $\delta^{18}O_{p,}$ with the wet season (JFM) values being more positive than the estimated drip water. The Texas site, CWN, displays the largest discrepancy between drip water estimated from speleothem $\delta^{18}O$ values and modeled $\delta^{18}O_{p,}$ as the estimates of drip water (using both fractionation relationships) are several per mil more positive than the modeled rainfall.

A comparison of the forward proxy model results, Karstolution and CaveCalc, and the measured stalagmite $\delta^{18}O$ from each cave site is presented in Figure 10 b. Karstolution runs result in a time series of output (Figure S3). For the purposes of comparison with CaveCalc and the speleothem values, we averaged the Karstolution time series and calculated the 1σ (standard deviation) of the mean. For Karstolution, we focus on the speleothem $\delta^{18}O$ estimates for Stalagmite 2 (short residence time) and Stalagmite 4 (long residence time). Stalagmite 2 displays more variability in the $\delta^{18}O$ time series than Stalagmite 4 (Figure S3) reflecting the short fluid residence time and thus has a larger standard deviation about the mean. Both the Karstolution Stalagmite 4, and the $\delta^{18}O$ estimate from CaveCalc fall within the standard deviation of the mean $\delta^{18}O$ of Stalagmite 2, indicating good agreement between the two forward proxy models used in this study for all cave sites, except COB. Further, the $\delta^{18}O$ estimate from CaveCalc agrees within the standard deviation of the mean $\delta^{18}O$ of the less variable Stalagmite 4 for all sites except COB. The CaveCalc estimate for COB is ~0.8‰ lower than the estimate for Stalagmite 4.

The CaveCalc and Karstolution estimates of $\delta^{18}O$ agree well with the measured speleothem

$\delta^{18}O$ for many of the sites. However, the measured stalagmite $\delta^{18}O$ at CWN is ~5‰ higher than the estimates from the proxy model runs, and stalagmite $\delta^{18}O$ at LSC is ~1‰ lower than the proxy model results. A comparison of the fully optimized Karstolution runs and the measured stalagmite $\delta^{18}O$ for cave sites LSC and ML is presented in Figure 10 c. The optimized output for Stalagmite 2 agrees with the measured speleothem $\delta^{18}O$ for LSC and ML. Additionally, the mean of the Stalagmite 4 $\delta^{18}O$ values agrees with measured $\delta^{18}O$ values in the ML stalagmite and is within 0.5‰ of the measured LSC speleothem $\delta^{18}O$ value. Thus, the forward proxy model results replicate well the measured stalagmite $\delta^{18}O$ values for the LGM from these cave sites, except for CWN, and the inclusion of cave monitoring results in the forward modeling process improves these comparisons.

4. Discussion

4.1 Simulation Comparison and Potential Biases

Our simulated pattern of hydrologic response at the LGM agrees with previous modeling works (e.g., Oster et al., 2015a; Lora et al., 2017; Morrill et al., 2018; Kageyama et al., 2020; Lofverstrom, 2020); the SW-US is generally wetter at the LGM and the NW-US is generally drier (Figure 1). Although this work is, to the best of our knowledge, the first to explicitly track North Pacific ETCs at the LGM, many of the mechanisms driving the change in W-US moisture agree with previous hypotheses. Like prior research, we find an equatorward shift and increase in North Pacific winter ETCs at the LGM (e.g., Yanase and Abe-Ouchi, 2007; Laîné et al., 2009; Figure 5). As recognized in previous works, this ETC response appears to be associated with both an increased horizontal temperature gradient due to cooling and a southward deflection/intensification of the low-level jet due to the presence of North American ice sheets

(e.g., Broccoli and Manabe, 1987; Wang et al., 2018; Figure 8; Figure 9). The results presented here further suggest that this increase in more southerly North Pacific ETCs during the winter allows more ETCs to advect low-latitude moisture, resulting in near-maintenance of present-day winter moisture transport close to the southwest coast despite significantly lower total precipitable water at the LGM. This response is partly attributable to AR activity as found previously (Lora et al., 2017). We also identify an important role for thermodynamically driven hydroclimate changes in the W-US at the LGM (Figure 6). The greater precipitation efficiency due to an enhanced horizontal temperature gradient from the North Pacific to the US interior has been identified in previous studies (e.g., Boos, 2012; Wong et al., 2015; Morrill et al., 2018). However, these previous works were unable to confirm the role of winter storm activity in maintaining moisture flux to the SW-US at the LGM due to the use of lower temporal resolution model data. Finally, our findings support some previous speculation on the role of changes in seasonality and storminess (e.g., Santi et al., 2020), with an increase in relatively depleted winter precipitation at the LGM in the Great Basin region.

From our sensitivity experiments, the moisture transport response to the W-US at the LGM is a product of both orographic and temperature changes (Figures 8). Although both factors increase winter ETC activity in the North Pacific, colder terrestrial surface temperature during the LGM primarily increases precipitation efficiency and only the response to LGM orography increases AR frequency. The impact of these drivers on W-US hydroclimate are dependent on somewhat uncertain boundary conditions. For example, our understanding of ice sheet topography has evolved significantly over the years (e.g., Abe-Ouchi et al., 2015). The spatial extent of the Laurentide ice sheet is well constrained by geological data, but the thickness and topographic elevation is more uncertain; the elevation of the ICE-6G topography used here is not as pronounced

as the ICE-5G topography (e.g., Peltier et al., 2015). Our results suggest that a more prominent Laurentide ice sheet, such as ICE-5G, may further displace south and increase winter ETC and AR activity in the North Pacific, as suggested by Lofverstrom et al. (2016). This may help explain the somewhat muted SW-US hydrologic response at the LGM in our and PMIP4 simulations relative to the mean from older PMIP simulations. Relatedly, we suspect that the amount of moisture transport is dependent on the Earth system sensitivity of the climate model. Although CESM1 has a non-linear Earth system sensitivity that generally performs well in paleoclimate simulations (e.g., Zhu et al., 2019; Feng et al., 2020), the LGM simulation presented here is cooler (~7.3°C global surface cooling relative to PI) than many other Earth system models and temperature reconstructions (e.g., Annan and Hargreaves, 2012; Shakun et al. 2012; Tierney et al., 2020; Kageyama et al., 2020). Regionally, we simulate 11.1°C of cooling in the central Sierra Nevada foothills at the LGM, which is significantly greater than a recently derived noble gas temperature difference of 5.2±1.7 °C (Wortham et al., in review). The region, however, contains a strong temperature gradient associated with steep and heterogenous topography. Higher horizontal resolution is therefore necessary to better compare models and proxies in this region. More generally, if iCESM1.3 overestimates cooling at the LGM, it likely underestimates North Pacific moisture and moisture transport. Concurrently, LGM cooling amplifies land-sea temperature contrast, which increases precipitation efficiency and reduces evaporation. Therefore, we cannot easily determine the hydroclimate and $\delta^{18}O_p$ biases caused by a possible surface temperature bias in our LGM simulation. That said, we may expect more precipitation in the W-US in a warmer LGM climate based on the findings from our sensitivity experiments. Finally, AR activity is likely impacted by LGM temperature and moisture transport. Unlike ETCs, ARs do not have a universal definition (Shields et al., 2018). It is possible that the cold North Pacific surface temperature in

our LGM simulation leads to bands of integrated vapor transport that do not reach the present-day-based threshold for classification as ARs (Lora et al., 2020). To an extent, we expect AR frequency to scale with background precipitable water and IVT based on our fixed parameters for AR identification. Techniques that use relative percentile IVT thresholds for AR detection may show an increase in AR frequency near the SW-US at the LGM (Rutz et al., 2019). When we reduce the thresholds for AR detection in TempestExtremes, we find an increase in AR frequency in parts of the North Pacific at the LGM relative to PI (Figure S10). This is a topic that requires future study using different thresholds and AR detection algorithms.

4.2 Interpreting proxies

Our simulations demonstrate that the general reduction in $\delta^{18}O_p$ in the W-US at the LGM is complex, driven primarily by greater precipitation efficiency and secondly by a greater portion of annual precipitation falling in the winter months around the Great Basin. These results agree well with the late glacial and LGM records of speleothem $\delta^{18}O$ from the W-US and help to reconcile the various interpretations of these records. In the interior SW-US, the stalagmites from both FS and COB display more negative $\delta^{18}O$ at the LGM than during the youngest part of the records, which is the end of the Younger Dryas (~11,500 years BP) (Figure 2). In both cases, this shift to more negative speleothem $\delta^{18}O$ during the LGM has been interpreted to reflect an increased contribution of relatively more negative winter precipitation (Asmerom et al., 2010; Wagner et al., 2010). Consistent with this interpretation, our simulations show an increase in winter precipitation across the study region, including the SW-US, at the LGM (Figure 7b). Our simulations further indicate that parts of the SW-US saw an increase in winter $\delta^{18}O_p$ values at the LGM as compared to the PI, but the overall mean annual $\delta^{18}O_p$ remains more negative at the LGM. For comparison,

our estimated LGM drip water (Figure 10 a) computed for both FS and COB most closely aligns with mean annual $\delta^{18}O_p$ from the iCESM1.3 experiments rather than wet season $\delta^{18}O_p$. Notably, for FS, the wettest 3 month period occurs in the summer for both the PI (MJJ) and the LGM (JJA), whereas at COB the wettest 3 month period occurs in the winter and early spring in both time slices (JFM).

In the Great Basin, more negative $\delta^{18}O$ values during the late glacial compared to the Holocene in LV speleothems have been interpreted to reflect a combination of colder glacial temperatures and changes in atmospheric circulation that potentially altered moisture source or rainout history of air masses reaching the LV caves (Lachniet et al., 2014). Our simulations add more detail to this interpretation, as they demonstrate that the more negative LGM $\delta^{18}O_p$ signal is a result of increased precipitation efficiency and rainout, as well as changes in the relative amount of moisture at the site. Furthermore, modeled winter precipitation greatly increases at LV, which also contributes to the lower $\delta^{18}O_p$ values. Like the SW-US caves, the estimated drip water from LV is also most closely aligned with mean annual rather than wet season (DJF) $\delta^{18}O_p$ indicated by the iCESM1.3 simulation (Figure 10 a).

Neither of the California speleothem records, LSC or ML, extend into the Holocene. However, the ML records show good agreement with the $\delta^{18}O$ record of the last deglaciation from nearby Moaning Cave (Oster et al., 2015b) which does extend into the early Holocene (Oster et al., 2009) and shows increasing $\delta^{18}O$ values relative to the late glacial ML record. The LSC record shows increased $\delta^{18}O$ values at the LGM relative to the deglacial part of that record (Figure 2b), and both records display smaller changes in $\delta^{18}O$ compared to the more inland LV, FS, and COB sites. These observations are consistent with our model results that show smaller negative or even positive $\delta^{18}O_p$ anomalies at the LGM along the coast (Figure 1a), and magnification of the negative

$\delta^{18}O_p$ inland as rainout increases. It has been hypothesized that increases in moisture from the CENP region at the LGM, relative to moisture from the North Pacific could have contributed to the higher speleothem $\delta^{18}O$ values at LSC (Oster et al., 2020). Indeed, our tagging results suggest that moisture from the CENP does increase at the LGM, and the increase in nearby moisture from CENP at the expense of more depleted moisture from the north and west limits depletion along the coast despite increased precipitation efficiency. At these more coastal sites, the mean annual and wet season $\delta^{18}O_p$ values are very similar and within 0.5‰ of the estimated drip water values for both caves.

The largest discrepancy between measured speleothem $\delta^{18}O$ during the late glacial and our model LGM results occurs at the CWN site in Texas. For this speleothem, late glacial $\delta^{18}O$ and the drip water estimated from it are several per mil more positive than the simulated LGM $\delta^{18}O_p$ from our iCESM1.3 experiments (Figure 10 a). Observations of rainfall from central Texas indicate that the primary source is the Gulf of Mexico (Pape et al., 2010), and the CWN stalagmite record has been interpreted primarily as a reflection of changing $\delta^{18}O$ of Gulf of Mexico surface waters with melting of the Laurentide Ice Sheet (Feng et al., 2014). Our comparison of modern measured rainfall $\delta^{18}O$ with modeled $\delta^{18}O_p$ from the PI simulation also suggests that measured precipitation is ~3‰ higher than the model output (Figure S1). This suggests a model bias. Nusbaumer et al. (2017) show that iCESM1 overestimates deep convection, resulting in a negative bias in $\delta^{18}O_p$. Unlike the W-US, which receives most of its precipitation from synoptic systems during the winter months, the CWN site receives a large portion of its annual precipitation from local convection during the spring and summer. This difference in portioning of precipitation type and season between regions may explain the depletion bias in iCESM1.3 at the CWN site. It is also possible that relatively enriched moisture from the Gulf of Mexico does not extend far enough

inland in the model. Either way, higher model resolution raises $\delta^{18}O_p$ at the CWN location by better resolving these features (Nusbaumer et al., 2017).

4.3 Model-Proxy Comparison Approaches

With the growing number of modeling groups running isotope-enabled paleoclimate models, there is increased attention toward developing protocols for comparing isotope-based proxy records to climate model output. Comas-Bru et al. (2019) proposed methods for comparing speleothem $\delta^{18}O$ to isotope-enabled model output, focusing on evaluating isotope anomalies between time slices and spatial patterns of variability between records and models in a given time slice. As most W-US speleothem records do not extend from the LGM to the present, precluding our ability to calculate anomalies, we focused on evaluating approaches for comparing the LGM speleothem $\delta^{18}O$ to the LGM iCESM1.3 output across this region. Following the strategy outlined in Comas-Bru et al. (2019), we computed estimated drip water values from the measured speleothem $\delta^{18}O$ and the modeled LGM temperature, evaluating both the Tremaine et al., (2011) empirical isotope fractionation factor and the equilibrium fractionation relationship of Kim & O'Neil (1996). Our results suggest that this approach of estimating LGM drip water results in a reasonable comparison with modeled $\delta^{18}O_p$. At most of our sites the estimated drip water value and the modeled $\delta^{18}O_p$ agree within ~0.5‰. Further, there is no clear evidence that one fractionation factor leads to closer agreement between the drip water estimates and modeled $\delta^{18}O_p$ (Figure 10 a). That said, the Kim & O'Neil (1996) equation consistently produces estimated drip water values that are higher and more fractionated from speleothem $\delta^{18}O$ values than the Tremaine et al. (2011) relationship.

Our results do suggest that applying a forward proxy model to the climate model output

supports robust comparisons between speleothem proxies and models, particularly for sites where the cave system is well characterized by monitoring data. Despite slightly different approaches, the two forward proxy models we utilized, CaveCalc and Karstolution, produce similar results, which is encouraging (Figure 10 b). One advantage of the Karstolution forward model is that it inputs the full time-series of climate model information for a given period, allowing the evaluation of the influence of mixing and water storage in the karst aquifer on the forward-modeled speleothem $\delta^{18}O_{p.}$ Although the time frame of the climate model output and Karstolution forward-modeled speleothem $\delta^{18}O$ time series (Figure S3) is much shorter than the amount of time included in our speleothem LGM estimates (500-1000 years), the forward-modeled speleothem time-series does support an evaluation of the temporal variability on a limited timescale as well as an assessment of the potential influence of seasonality on these records. An understanding of seasonal cave ventilation from monitoring can improve future proxy-model comparison as the Karstolution model can be appropriately tuned. Likewise, an understanding of water-residence time in the epikarst of the cave(s) of interest can help determine which forward-modeled stalagmite is the more appropriate comparison. However, our results also demonstrate that when cave monitoring data are not available, both Karstolution and CaveCalc produce reasonable comparisons with the measured speleothem values using default settings. Further, if monthly time-series are not available as climate model output, CaveCalc, which accepts mean annual values for the necessary parameters, also produces reasonable results.

4.4 Final Thoughts: Reconciling existing mechanisms for the W-US

Putting our findings in the context of prior hypotheses, we find that the hydroclimate response in the W-US at the LGM is the result of several previously identified mechanisms. Like

prior studies, we observe a southward displacement and intensification of the North Pacific low-level jet stream, driven primarily by the presence of LGM ice sheets (e.g., Wang et al., 2018). Extratropical cyclone activity associated with a stronger latitudinal surface temperature gradient and enhanced jet in the North Pacific lead to a greater number of more southerly storms impacting the W-US at the LGM during the winter months (e.g., Laîné et al., 2009). As a result of these factors, winter moisture transport into the SW-US is only slightly reduced, despite significantly less atmospheric water vapor due to cooler temperatures at the LGM. AR activity also plays a role in maintaining SW-US moisture transport at the LGM but the magnitude of contribution likely depends on AR identification choices (Lora et al., 2017). In the SW-US, continued moisture input from the subtropics in combination with greater precipitation efficiency from increased land-sea contrast leads to enhanced winter precipitation at the LGM (e.g., Boos, 2012); reduced evaporation enhances this moistening. In the NW-US, the reduction in atmospheric water vapor and its transport by the low-level jet and ETCs, in concert with entrainment of dry, stable air from the North American ice sheets, results in reduced precipitation at LGM in the winter months. In addition, summer precipitation generally decreases in the W-US at the LGM, especially in regions with significant convective precipitation. Overall, this combination of dynamic and thermodynamic changes at the LGM result in wetter conditions in the SW-US and drier conditions in the NW-US.

The simulated annual and winter $\delta^{18}O_p$ changes in the W-US at the LGM do not reflect the pattern of wetting and drying, but the mechanisms governing both are related. The $\delta^{18}O_p$ changes at the LGM are primarily driven by responses in precipitation efficiency and rainout followed by seasonality, with greater precipitation efficiency leading to isotopic depletion throughout the W-US and more winter precipitation leading to isotopic depletion around the Great Basin region.

Enhanced rainout at the LGM results in more depletion as moisture moves into the continental interior, which agrees with speleothem $\delta^{18}O$. In contrast, atmospheric circulation and moisture availability play a larger role in the precipitation responses in the W-US at the LGM. Understanding the mechanisms responsible for the differences between precipitation and $\delta^{18}O_p$ can tell us about unique aspects of past climate change. Based on our results, speleothem $\delta^{18}O$ records of the W-US may provide a distinct signature of climate change at the LGM, which complements other hydroclimate proxies such as lake and pollen records. Through appreciating the complexities of water isotopic reconstructions, we can produce a more complete picture of past hydroclimate change. Improved model resolution and surface boundary conditions will be important next steps for reconciling regionally variability found in proxy records of the W-US at the LGM.

Acknowledgements:

The authors thank Juan Lora for discussion about and assistance with atmospheric river tracking. The CESM project is supported primarily by the National Science Foundation (NSF). This material is based upon work supported by the National Center for Atmospheric Research, which is a major facility sponsored by the NSF under Cooperative Agreement No. 1852977. Computing and data storage resources, including the Cheyenne supercomputer (doi:10.5065/D6RX99HX), were provided by the Computational and Information Systems Laboratory (CISL) at NCAR. Data used in this manuscript are available by email request to the corresponding author. We thank editor Ingrid Hendy for handling our manuscript and the thoughtful comments of two anonymous reviewers.

Funding:

This work was supported by NSF grants AGS-1804747 to Tabor and Montañez, AGS-1554998 to Oster, and AGS-1810682 to Liu.

References:

Abe-Ouchi, A., Saito, F., Kageyama, M., Braconnot, P., Harrison, S. P., Lambeck, K., ... & Takahashi, K. (2015). Ice-sheet configuration in the CMIP5/PMIP3 Last Glacial Maximum experiments. *Geoscientific Model Development*, *8*(11), 3621-3637.

Asmerom, Y., Polyak, V. J., & Burns, S. J. (2010). Variable winter moisture in the southwestern United States linked to rapid glacial climate shifts. *Nature Geoscience*, *3*(2), 114-117.

Baker, A. J., Mattey, D. P., & Baldini, J. U. (2014). Reconstructing modern stalagmite growth from cave monitoring, local meteorology, and experimental measurements of dripwater films. *Earth and Planetary Science Letters*, *392*, 239-249.

Baker, A., & Bradley, C. (2010). Modern stalagmite δ18O: Instrumental calibration and forward modelling. *Global and Planetary change*, *71*(3-4), 201-206.

Baker, A., Bradley, C., Phipps, S. J., Fischer, M., Fairchild, I. J., Fuller, L., ... & Azcurra, C. (2012). Millennial-length forward models and pseudoproxies of stalagmite δ 18 O: an example from NW Scotland. *Climate of the Past*, *8*(4), 1153-1167.

Bartlein, P. J., Harrison, S. P., Brewer, S., Connor, S., Davis, B. A. S., Gajewski, K., ... & Wu, H. (2011). Pollen-based continental climate reconstructions at 6 and 21 ka: a global synthesis. *Climate Dynamics*, *37*(3), 775-802.

Bereiter, B., Eggleston, S., Schmitt, J., Nehrbass-Ahles, C., Stocker, T. F., Fischer, H., ... & Chappellaz, J. (2015). Revision of the EPICA Dome C CO2 record from 800 to 600 kyr before present. *Geophysical Research Letters*, *42*(2), 542-549.

Bhattacharya, T., Tierney, J. E., & DiNezio, P. (2017). Glacial reduction of the North American Monsoon via surface cooling and atmospheric ventilation. *Geophysical Research Letters*, *44*(10), 5113-5122.

Boos, W. R. (2012). Thermodynamic scaling of the hydrological cycle of the Last Glacial Maximum. *Journal of Climate*, *25*(3), 992-1006.

Bradley, C., Baker, A., Jex, C. N., & Leng, M. J. (2010). Hydrological uncertainties in the modelling of cave drip-water δ18O and the implications for stalagmite palaeoclimate reconstructions. *Quaternary Science Reviews*, *29*(17-18), 2201-2214.

Brady, E., Stevenson, S., Bailey, D., Liu, Z., Noone, D., Nusbaumer, J., ... & Zhu, J. (2019). The connected isotopic water cycle in the Community Earth System Model version 1. *Journal of Advances in Modeling Earth Systems*, *11*(8), 2547-2566.

Broccoli, A. J., & Manabe, S. (1987). The influence of continental ice, atmospheric CO 2, and land albedo on the climate of the last glacial maximum. *Climate dynamics*, 1(2), 87-99.

Buenning, N. H., Stott, L., Yoshimura, K., & Berkelhammer, M. (2012). The cause of the seasonal variation in the oxygen isotopic composition of precipitation along the western US coast. *Journal of Geophysical Research: Atmospheres*, *117*(D18).

Chang, E. K., Zheng, C., Lanigan, P., Yau, A. M., & Neelin, J. D. (2015). Significant modulation of variability and projected change in California winter precipitation by extratropical cyclone activity. *Geophysical Research Letters*, *42*(14), 5983-5991.

Cohmap Members. (1988). Climatic changes of the last 18,000 years: observations and model simulations. *Science*, 1043-1052.

Comas-Bru, L., Atsawawaranunt, K., & Harrison, S. (2020). SISAL (Speleothem Isotopes Synthesis and AnaLysis Working Group) database version 2.0.

Comas-Bru, L., Harrison, S. P., Werner, M., Rehfeld, K., Scroxton, N., & Veiga-Pires, C. (2019). Evaluating model outputs using integrated global speleothem records of climate change since the last glacial. *Climate of the Past*, *15*(4), 1557-1579.

Deininger, M., Fohlmeister, J., Scholz, D., & Mangini, A. (2012). Isotope disequilibrium effects: The influence of evaporation and ventilation effects on the carbon and oxygen isotope composition of speleothems–A model approach. *Geochimica et Cosmochimica Acta*, *96*, 57-79.

Dettinger, M. D., Cayan, D. R., Diaz, H. F., & Meko, D. M. (1998). North–south precipitation patterns in western North America on interannual-to-decadal timescales. *Journal of Climate*, *11*(12), 3095-3111.

Dettinger, M., Udall, B., & Georgakakos, A. (2015). Western water and climate change. *Ecological Applications*, *25*(8), 2069-2093.

Diffenbaugh, N. S., Swain, D. L., & Touma, D. (2015). Anthropogenic warming has increased drought risk in California. *Proceedings of the National Academy of Sciences*, *112*(13), 3931-3936.

Duplessy, J. C., Labeyrie, L., & Waelbroeck, C. (2002). Constraints on the ocean oxygen isotopic enrichment between the Last Glacial Maximum and the Holocene: Paleoceanographic implications. *Quaternary Science Reviews*, *21*(1-3), 315-330.

Fairchild, I. J., Smith, C. L., Baker, A., Fuller, L., Spötl, C., Mattey, D., & McDermott, F. (2006). Modification and preservation of environmental signals in speleothems. *Earth-Science Reviews*, *75*(1-4), 105-153.

Feakins, S. J., Wu, M. S., Ponton, C., & Tierney, J. E. (2019). Biomarkers reveal abrupt switches in hydroclimate during the last glacial in southern California. *Earth and Planetary Science Letters*, *515*, 164-172.

Feng, R., Otto-Bliesner, B. L., Brady, E. C., & Rosenbloom, N. (2020). Increased climate response and earth system sensitivity from CCSM4 to CESM2 in mid-Pliocene simulations. *Journal of Advances in Modeling Earth Systems*, *12*(8), e2019MS002033.

Feng, W., Casteel, R. C., Banner, J. L., & Heinze-Fry, A. (2014). Oxygen isotope variations in rainfall, drip-water and speleothem calcite from a well-ventilated cave in Texas, USA: Assessing a new speleothem temperature proxy. *Geochimica et Cosmochimica Acta*, *127*, 233-250.

Guan, B., & Waliser, D. E. (2015). Detection of atmospheric rivers: Evaluation and application of an algorithm for global studies. *Journal of Geophysical Research: Atmospheres*, *120*(24), 12514-12535.

Guo, Y., Shinoda, T., Guan, B., Waliser, D. E., & Chang, E. K. (2020). Statistical relationship between atmospheric rivers and extratropical cyclones and anticyclones. *Journal of Climate*, *33*(18), 7817-7834.

Hamlet, A. F., & Lettenmaier, D. P. (2007). Effects of 20th century warming and climate variability on flood risk in the western US. *Water Resources Research*, *43*(6).

Hargreaves, J. C., Annan, J. D., Yoshimori, M., & Abe-Ouchi, A. (2012). Can the Last Glacial Maximum constrain climate sensitivity?. *Geophysical Research Letters*, *39*(24).

He, C., Liu, Z., Otto-Bliesner, B. L., Brady, E. C., Zhu, C., Tomas, R., ... & Bao, Y. (2021). Hydroclimate footprint of pan-Asian monsoon water isotope during the last deglaciation. *Science Advances*, *7*(4), eabe2611.

Hudson, A. M., Hatchett, B. J., Quade, J., Boyle, D. P., Bassett, S. D., Ali, G., & Marie, G. (2019). North-south dipole in winter hydroclimate in the western United States during the last deglaciation. *Scientific reports*, *9*(1), 1-12.

Hurrell, J. W., Holland, M. M., Gent, P. R., Ghan, S., Kay, J. E., Kushner, P. J., ... & Marshall, S. (2013). The community earth system model: a framework for collaborative research. *Bulletin of the American Meteorological Society*, *94*(9), 1339-1360.

Kageyama, M., Albani, S., Braconnot, P., Harrison, S. P., Hopcroft, P. O., Ivanovic, R. F., ... & Zheng, W. (2017). The PMIP4 contribution to CMIP6–Part 4: Scientific objectives and experimental design of the PMIP4-CMIP6 Last Glacial Maximum experiments and PMIP4 sensitivity experiments. *Geoscientific Model Development*, *10*(11), 4035-4055.

Kageyama, M., Harrison, S. P., Kapsch, M. L., Lofverstrom, M., Lora, J. M., Mikolajewicz, U., ... & Zhu, J. (2021). The PMIP4 Last Glacial Maximum experiments: preliminary results and comparison with the PMIP3 simulations. *Climate of the Past*, *17*(3), 1065-1089.

Kim, S. T., & O'Neil, J. R. (1997). Equilibrium and nonequilibrium oxygen isotope effects in synthetic carbonates. *Geochimica et cosmochimica acta*, *61*(16), 3461-3475.

Kottek, M., Grieser, J., Beck, C., Rudolf, B., & Rubel, F. (2006). World map of the Köppen-Geiger climate classification updated.

Lachniet, M. S., Denniston, R. F., Asmerom, Y., & Polyak, V. J. (2014). Orbital control of western North America atmospheric circulation and climate over two glacial cycles. *Nature communications*, *5*(1), 1-8.

Laîné, A., Kageyama, M., Salas-Mélia, D., Voldoire, A., Riviere, G., Ramstein, G., ... & Peterschmitt, J. Y. (2009). Northern hemisphere storm tracks during the last glacial maximum in the PMIP2 ocean-atmosphere coupled models: energetic study, seasonal cycle, precipitation. *Climate Dynamics*, *32*(5), 593-614.

Laskar, J., Fienga, A., Gastineau, M., & Manche, H. (2011). La2010: a new orbital solution for the long-term motion of the Earth. *Astronomy & Astrophysics*, *532*, A89.

LeGrande, A. N., & Schmidt, G. A. (2006). Global gridded data set of the oxygen isotopic composition in seawater. *Geophysical research letters*, *33*(12).

Lofverstrom, M. (2020). A dynamic link between high-intensity precipitation events in southwestern North America and Europe at the Last Glacial Maximum. *Earth and Planetary Science Letters*, *534*, 116081.

Löfverström, M., & Liakka, J. (2016). On the limited ice intrusion in Alaska at the LGM. *Geophysical Research Letters*, *43*(20), 11-030.

Löfverström, M., Caballero, R., Nilsson, J., & Messori, G. (2016). Stationary wave reflection as a mechanism for zonalizing the Atlantic winter jet at the LGM. *Journal of the Atmospheric Sciences*, *73*(8), 3329-3342.

Lora, J. M. (2018). Components and mechanisms of hydrologic cycle changes over North America at the Last Glacial Maximum. *Journal of Climate*, *31*(17), 7035-7051.

Lora, J. M., Mitchell, J. L., Risi, C., & Tripati, A. E. (2017). North Pacific atmospheric rivers and their influence on western North America at the Last Glacial Maximum. *Geophysical Research Letters*, *44*(2), 1051-1059.

Lora, J. M., Shields, C. A., & Rutz, J. J. (2020). Consensus and disagreement in atmospheric river detection: ARTMIP global catalogues. *Geophysical Research Letters*, *47*(20), e2020GL089302.

Lyle, M., Heusser, L., Ravelo, C., Yamamoto, M., Barron, J., Diffenbaugh, N. S., ... & Andreasen, D. (2012). Out of the tropics: the Pacific, Great Basin Lakes, and Late Pleistocene water cycle in the western United States. *science*, *337*(6102), 1629-1633.

Manabe, S., & Broccoli, A. J. (1985). The influence of continental ice sheets on the climate of an ice age. *Journal of Geophysical Research: Atmospheres*, *90*(D1), 2167-2190.

Morrill, C., Lowry, D. P., & Hoell, A. (2018). Thermodynamic and dynamic causes of pluvial conditions during the Last Glacial Maximum in western North America. *Geophysical Research Letters*, *45*(1), 335-345.

Nusbaumer, J., Wong, T. E., Bardeen, C., & Noone, D. (2017). Evaluating hydrological processes in the C ommunity A tmosphere M odel V ersion 5 (C AM5) using stable isotope ratios of water. *Journal of Advances in Modeling Earth Systems*, *9*(2), 949-977.

Oster, J. L., & Kelley, N. P. (2016). Tracking regional and global teleconnections recorded by western North American speleothem records. *Quaternary Science Reviews*, *149*, 18-33.

Oster, J. L., Ibarra, D. E., Winnick, M. J., & Maher, K. (2015). Steering of westerly storms over western North America at the Last Glacial Maximum. *Nature Geoscience*, *8*(3), 201-205.

Oster, J. L., Montañez, I. P., & Kelley, N. P. (2012). Response of a modern cave system to large seasonal precipitation variability. *Geochimica et Cosmochimica Acta*, *91*, 92-108.

Oster, J. L., Montanez, I. P., Santare, L. R., Sharp, W. D., Wong, C., & Cooper, K. M. (2015). Stalagmite records of hydroclimate in central California during termination 1. *Quaternary Science Reviews*, *127*, 199-214.

Oster, J. L., Montañez, I. P., Sharp, W. D., & Cooper, K. M. (2009). Late Pleistocene California droughts during deglaciation and Arctic warming. *Earth and Planetary Science Letters*, *288*(3-4), 434-443.

Oster, J. L., Warken, S. F., Sekhon, N., Arienzo, M. M., & Lachniet, M. (2019). Speleothem paleoclimatology for the caribbean, Central America, and north America. *Quaternary*, *2*(1), 5.

Oster, J. L., Weisman, I. E., & Sharp, W. D. (2020). Multi-proxy stalagmite records from northern California reveal dynamic patterns of regional hydroclimate over the last glacial cycle. *Quaternary Science Reviews*, *241*, 106411.

Owen, R., Day, C. C., & Henderson, G. M. (2018). CaveCalc: A new model for speleothem chemistry & isotopes. *Computers & Geosciences*, *119*, 115-122.

Pape, J. R., Banner, J. L., Mack, L. E., Musgrove, M., & Guilfoyle, A. (2010). Controls on oxygen isotope variability in precipitation and cave drip waters, central Texas, USA. *Journal of Hydrology*, *385*(1-4), 203-215.

Pausata, F. S., & Löfverström, M. (2015). On the enigmatic similarity in Greenland δ18O between the Oldest and Younger Dryas. *Geophysical Research Letters*, *42*(23), 10-470.

Pausata, F. S., Battisti, D. S., Nisancioglu, K. H., & Bitz, C. M. (2011). Chinese stalagmite δ 18 O controlled by changes in the Indian monsoon during a simulated Heinrich event. *Nature Geoscience*, *4*(7), 474-480.

Peltier, W. R., Argus, D. F., & Drummond, R. (2015). Space geodesy constrains ice age terminal deglaciation: The global ICE-6G_C (VM5a) model. *Journal of Geophysical Research: Solid Earth*, *120*(1), 450-487.

Rehfeld, K., Hébert, R., Lora, J. M., Lofverstrom, M., & Brierley, C. M. (2020). Variability of surface climate in simulations of past and future. *Earth System Dynamics*, *11*(2), 447-468.

Rhoades, A. M., Jones, A. D., Srivastava, A., Huang, H., O'Brien, T. A., Patricola, C. M., ... & Zhou, Y. (2020). The shifting scales of western US landfalling atmospheric rivers under climate change. *Geophysical Research Letters*, *47*(17), e2020GL089096.
Rhoades, A. M., Jones, A. D., Srivastava, A., Huang, H., O'Brien, T. A., Patricola, C. M., ... & Zhou, Y. (2020). The shifting scales of western US landfalling atmospheric rivers under climate change. *Geophysical Research Letters*, *47*(17), e2020GL089096.
Rhoades, A. M., Risser, M. D., Stone, D. A., Wehner, M. F., & Jones, A. D. (2021). Implications of warming on western United States landfalling atmospheric rivers and their flood damages. *Weather and Climate Extremes*, *32*, 100326.

Routson, C. C., McKay, N. P., Kaufman, D. S., Erb, M. P., Goosse, H., Shuman, B. N., ... & Ault, T. (2019). Mid-latitude net precipitation decreased with Arctic warming during the Holocene. *Nature*, *568*(7750), 83-87.

Rutz, J. J., Shields, C. A., Lora, J. M., Payne, A. E., Guan, B., Ullrich, P., ... & Viale, M. (2019). The atmospheric river tracking method intercomparison project (ARTMIP): quantifying uncertainties in atmospheric river climatology. *Journal of Geophysical Research: Atmospheres*, *124*(24), 13777-13802.

Santi, L. M., Arnold, A. J., Ibarra, D. E., Whicker, C. A., Mering, J. A., Lomarda, R. B., ... & Tripati, A. (2020). Clumped isotope constraints on changes in latest Pleistocene hydroclimate in the northwestern Great Basin: Lake Surprise, California. *GSA Bulletin*, *132*(11-12), 2669-2683.

Seager, R., Ting, M., Held, I., Kushnir, Y., Lu, J., Vecchi, G., ... & Naik, N. (2007). Model projections of an imminent transition to a more arid climate in southwestern North America. *Science*, *316*(5828), 1181-1184.

Shakun, J. D., Clark, P. U., He, F., Marcott, S. A., Mix, A. C., Liu, Z., ... & Bard, E. (2012). Global warming preceded by increasing carbon dioxide concentrations during the last deglaciation. *Nature*, *484*(7392), 49-54.

Shields, C. A., Kiehl, J. T., Rush, W., Rothstein, M., & Snyder, M. A. (2021). Atmospheric rivers in high-resolution simulations of the Paleocene Eocene Thermal Maximum (PETM). *Palaeogeography, Palaeoclimatology, Palaeoecology*, *567*, 110293.

Shields, C. A., Rutz, J. J., Leung, L. Y., Ralph, F. M., Wehner, M., Kawzenuk, B., ... & Nguyen, P. (2018). Atmospheric river tracking method intercomparison project (ARTMIP): project goals and experimental design. *Geoscientific Model Development*, *11*(6), 2455-2474.

Skinner, C. B., Lora, J. M., Payne, A. E., & Poulsen, C. J. (2020). Atmospheric river changes shaped mid-latitude hydroclimate since the mid-Holocene. *Earth and Planetary Science Letters*, *541*, 116293.

Swain, D. L., Langenbrunner, B., Neelin, J. D., & Hall, A. (2018). Increasing precipitation volatility in twenty-first-century California. *Nature Climate Change*, *8*(5), 427-433.

Tabor, C. R., Otto-Bliesner, B. L., Brady, E. C., Nusbaumer, J., Zhu, J., Erb, M. P., ... & Noone, D. (2018). Interpreting precession-driven δ18O variability in the South Asian monsoon region. *Journal of Geophysical Research: Atmospheres*, *123*(11), 5927-5946.

Tierney, J. E., Zhu, J., King, J., Malevich, S. B., Hakim, G. J., & Poulsen, C. J. (2020). Glacial cooling and climate sensitivity revisited. *Nature*, *584*(7822), 569-573.

Treble, A., Hasan, K. M., Iftikhar, A., Stuebing, K. K., Kramer, L. A., Cox Jr, C. S., ... & Ewing-Cobbs, L. (2013). Working memory and corpus callosum microstructural integrity after pediatric traumatic brain injury: a diffusion tensor tractography study. *Journal of neurotrauma*, *30*(19), 1609-1619.

Treble, P., Mah, M., Griffiths, A. D., Baker, A., Deininger, M., Kelly, B., ... & Hankin, S. (2019). Separating isotopic impacts of karst and in-cave processes from climate variability using an integrated speleothem isotope-enabled forward model.

Tremaine, D. M., Froelich, P. N., & Wang, Y. (2011). Speleothem calcite farmed in situ: Modern calibration of δ18O and δ13C paleoclimate proxies in a continuously-monitored natural cave system. *Geochimica et Cosmochimica Acta*, *75*(17), 4929-4950.

Ullrich, P. A., & Zarzycki, C. M. (2017). TempestExtremes: A framework for scale-insensitive pointwise feature tracking on unstructured grids. *Geoscientific Model Development*, *10*(3), 1069-1090.

Ullrich, P. A., Zarzycki, C. M., McClenny, E. E., Pinheiro, M. C., Stansfield, A. M., & Reed, K. A. (2021). TempestExtremes v2. 1: a community framework for feature detection, tracking and analysis in large datasets. *Geoscientific Model Development Discussions*, 1-37.

US Bureau of Economic Analysis (2020). Gross Domestic Product by State, 4th Quarter and Annual 2020.

US Census Bureau (2020). Population, Population Change, and Estimated Components of Population Change: April 1, 2010 to July 1, 2019.

Wagner, J. D., Cole, J. E., Beck, J. W., Patchett, P. J., Henderson, G. M., & Barnett, H. R. (2010). Moisture variability in the southwestern United States linked to abrupt glacial climate change. *Nature Geoscience*, *3*(2), 110-113.

Wang, N., Jiang, D., & Lang, X. (2018). Northern westerlies during the Last Glacial Maximum: Results from CMIP5 simulations. *Journal of Climate*, *31*(3), 1135-1153.

Wong, C. I., Potter, G. L., Montañez, I. P., Otto-Bliesner, B. L., Behling, P., & Oster, J. L. (2016). Evolution of moisture transport to the western US during the last deglaciation. *Geophysical Research Letters*, *43*(7), 3468-3477.

Wortham, B.E., Mukhopadhyay, S., Montañez, I.P., Middleton, J., Tyra, A. in revision. A 5 °C cooling in Western Sierra Nevada, California, recorded in stalagmite noble gas concentrations during the Last Glacial Maximum. *Earth and Planetary Science Letters.*

Yanase, W., & Abe-Ouchi, A. (2007). The LGM surface climate and atmospheric circulation over East Asia and the North Pacific in the PMIP2 coupled model simulations. *Climate of the Past*, *3*(3), 439-451.

Zarzycki, C. M. (2018). Projecting changes in societally impactful northeastern US snowstorms. *Geophysical Research Letters*, *45*(21), 12-067.

Zhu, J., Liu, Z., Brady, E., Otto-Bliesner, B., Zhang, J., Noone, D., ... & Tabor, C. (2017). Reduced ENSO variability at the LGM revealed by an isotope-enabled Earth system model. *Geophysical Research Letters*, *44*(13), 6984-6992.

Zhu, J., Poulsen, C. J., & Tierney, J. E. (2019). Simulation of Eocene extreme warmth and high climate sensitivity through cloud feedbacks. *Science advances*, *5*(9), eaax1874.

Zhu, Y., & Newell, R. E. (1998). A proposed algorithm for moisture fluxes from atmospheric rivers. *Monthly weather review*, *126*(3), 725-735.

Supplemental:

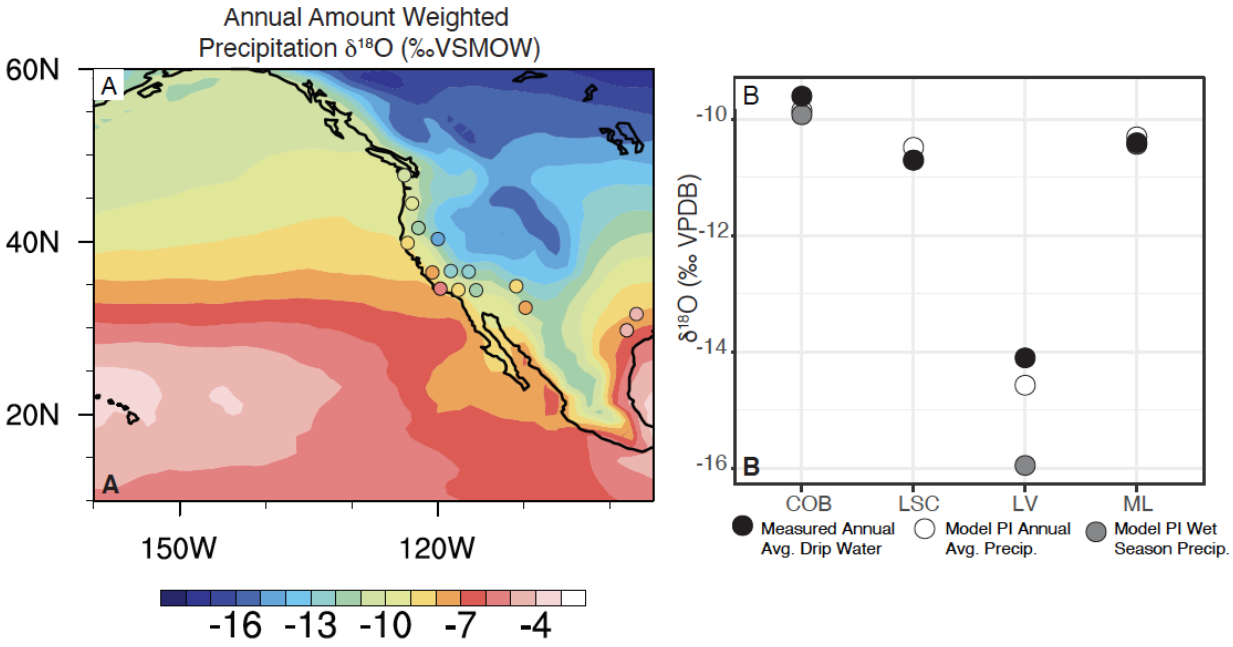

Figure S1: A) Annual amount weighted $\delta^{18}O_p$ of precipitation for the PI simulation of iCESM1.3 (background map) compared to annual amount weighted $\delta^{18}O_p$ measured at several GNIP (www.iaea.org) and National Air Deposition Program (NADP) collection sites in the W-US (Buenning et al., 2012; Oster et al., 2020). B) For W-US cave sites included in this study with published drip water $\delta^{18}O$ data (Wagner et al., 2010; Oster et al., 2012; Lachniet et al., 2014; Oster et al., 2020): a comparison of mean annual drip water $\delta^{18}O$ with annual and wet season amount weighted annual precipitation $\delta^{18}O$ for the PI simulation of iCESM1.3 for the grid cell in which each cave is located.

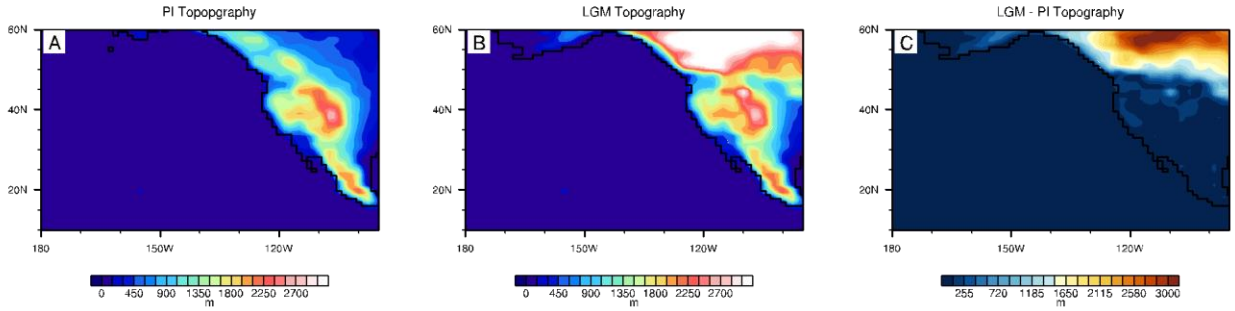

Figure S2: Topography of the western United States. A) Surface elevation from the preindustrial simulation. B) Surface elevation from the LGM simulation.

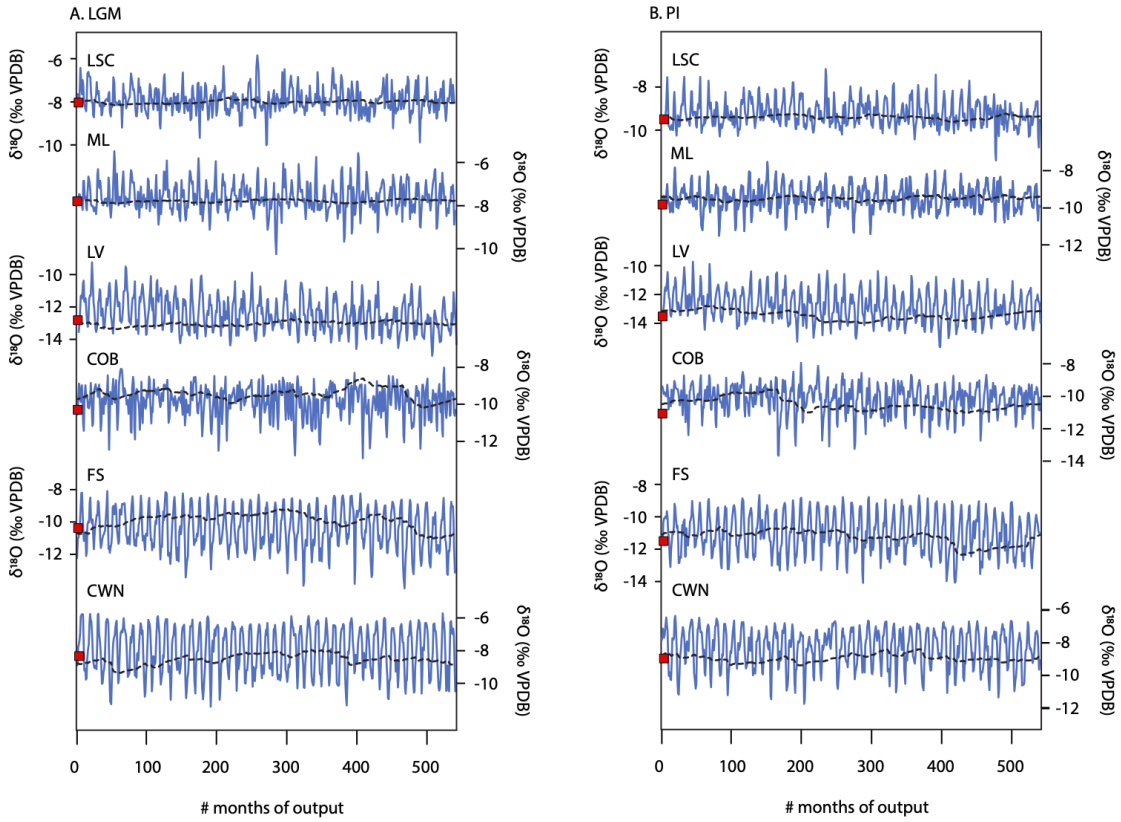

Figure S3: Karstolution time series and CaveCalc estimates. The monthly time series output for stalagmite $\delta^{18}O$ (per mil; VPDB) is presented for six cave sites (top to bottom: LSC, ML, LV, COB, FS, CWN) from Stalagmite 2 (blue line) and Stalagmite 4 (black dashed line). The time series of estimates is compared to the estimate of stalagmite $\delta^{18}O$ from CaveCalc (red square). The forward proxy system models were run for (A) the LGM and (B) the PI. The full time series of speleothem $\delta^{18}O$from the Karstolution proxy system model are compared to the CaveCalc estimate of speleothem $\delta^{18}O$ (Supp. Fig. X) for each cave site that was considered (LSC, Oster et al., 2020; ML, Oster et al., 2015; COB, Wagner et al., 2010; LV, Lachniet et al., 2012; 2014; FS, Asmerom et al., 2010; CWN, Feng et al., 2014). The temporal resolution and length of the output from Karstolution matches the input.

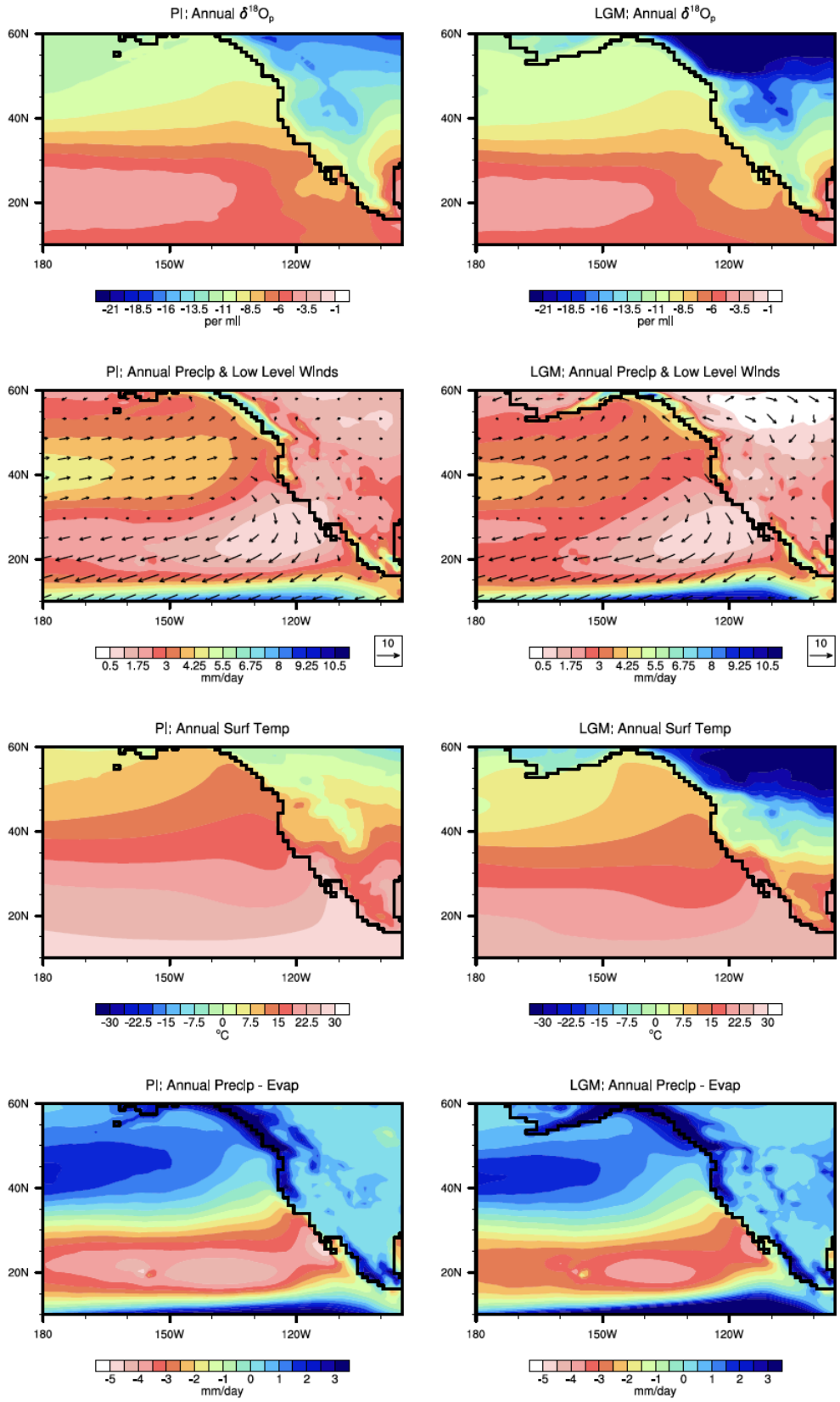

Figure S4: Same variables as Figure 1 but for PI (left column) and LGM (right column).

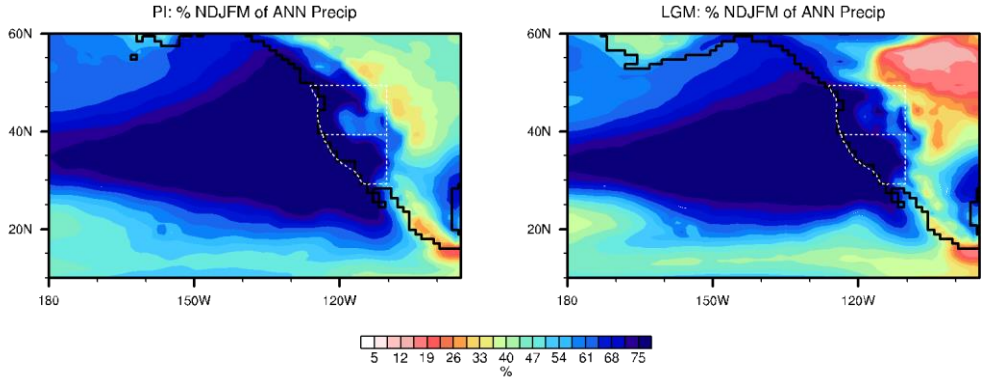

Figure S5: Contributions to annual precipitation from winter precipitation. A) Percent of annual precipitation from winter (Nov-Mar) precipitation in the PI simulation. B) Percent of annual precipitation from winter (Nov-Mar) precipitation in the LGM simulation. Northwest and Southwest United States regions outlined with dashed white lines. LGM continental configuration outlined in black.

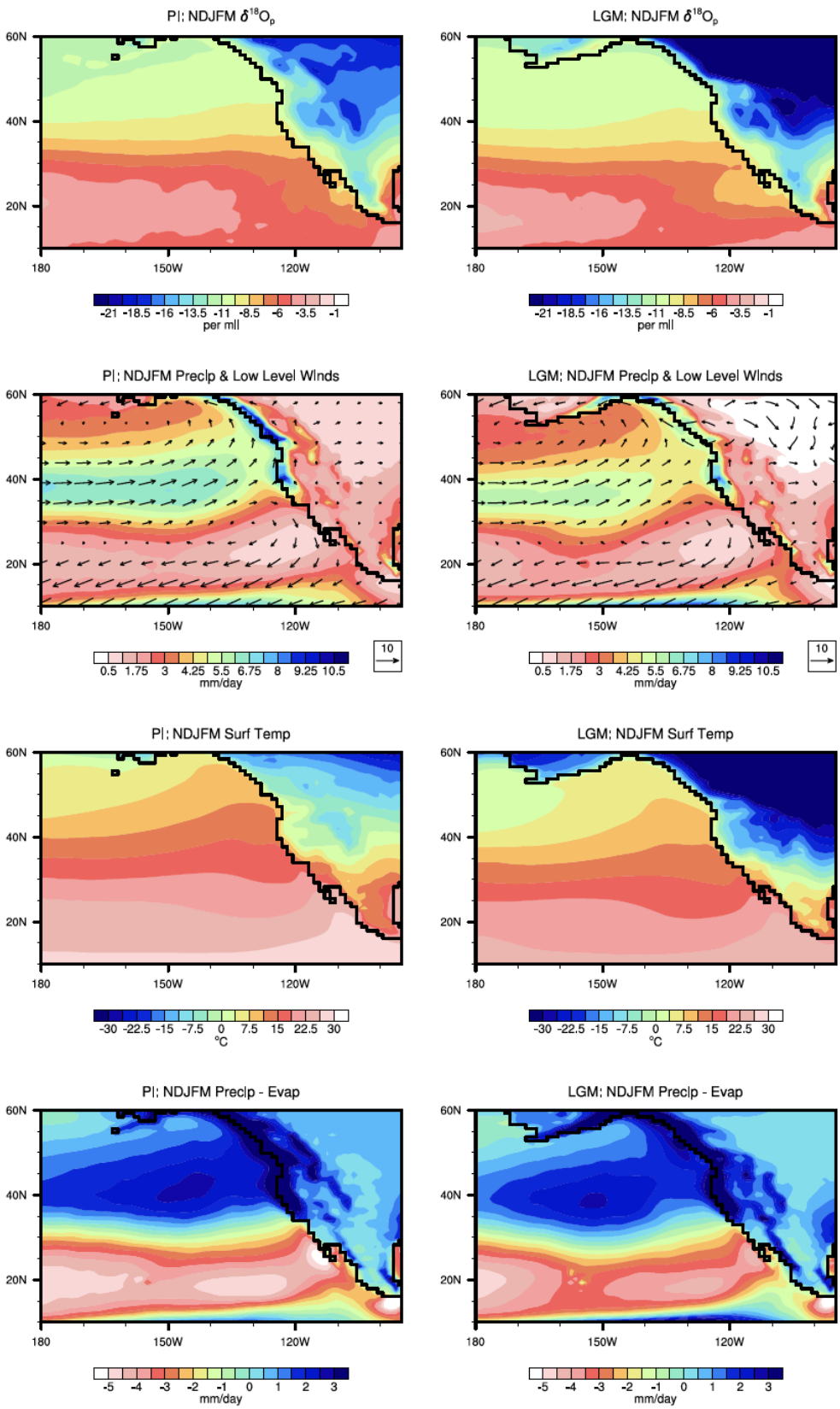

Figure S6: Same variables as Figure 3 but for PI (left column) and LGM (right column).

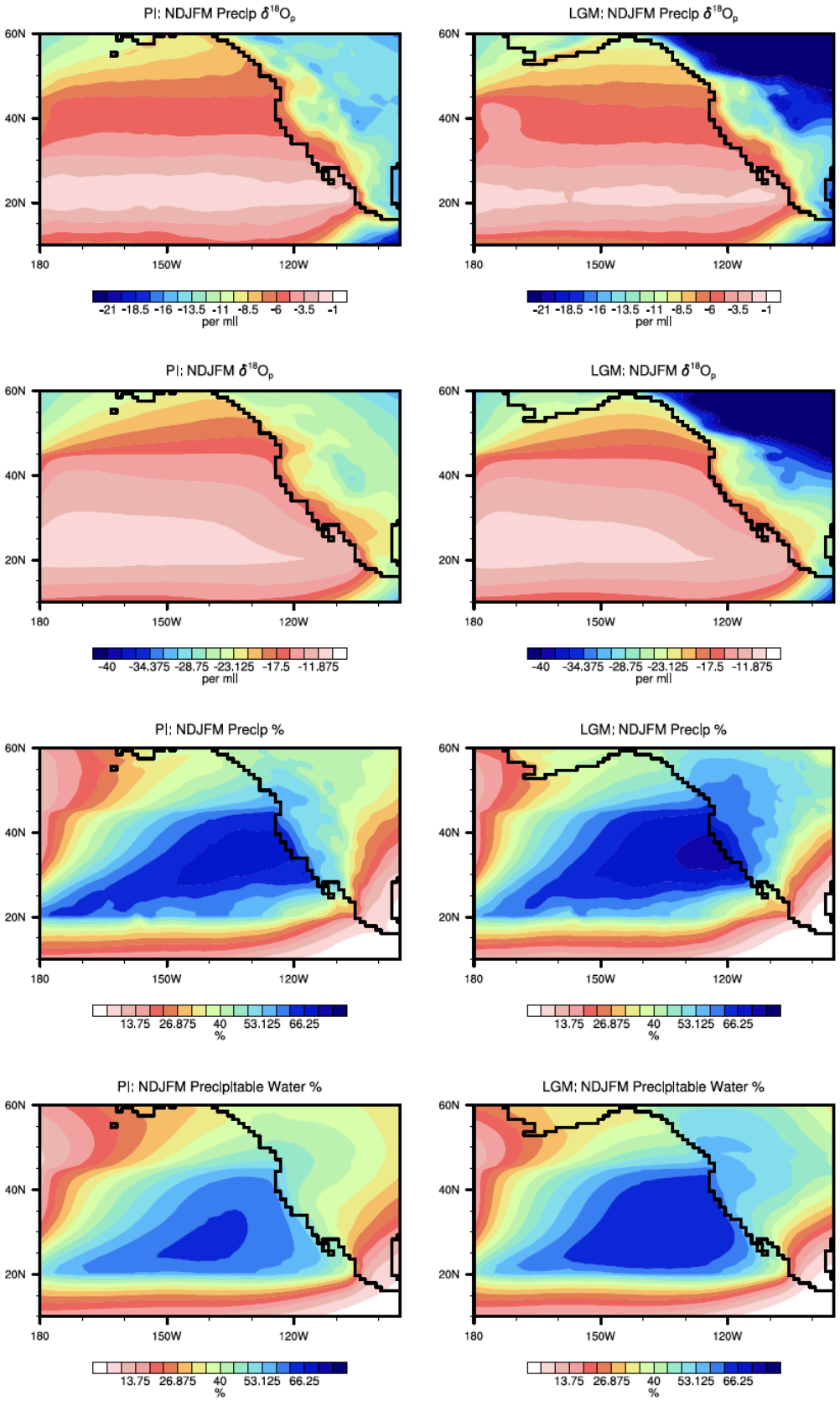

Figure S7: Same variables as Figure 4 but for PI (left column) and LGM (right column).

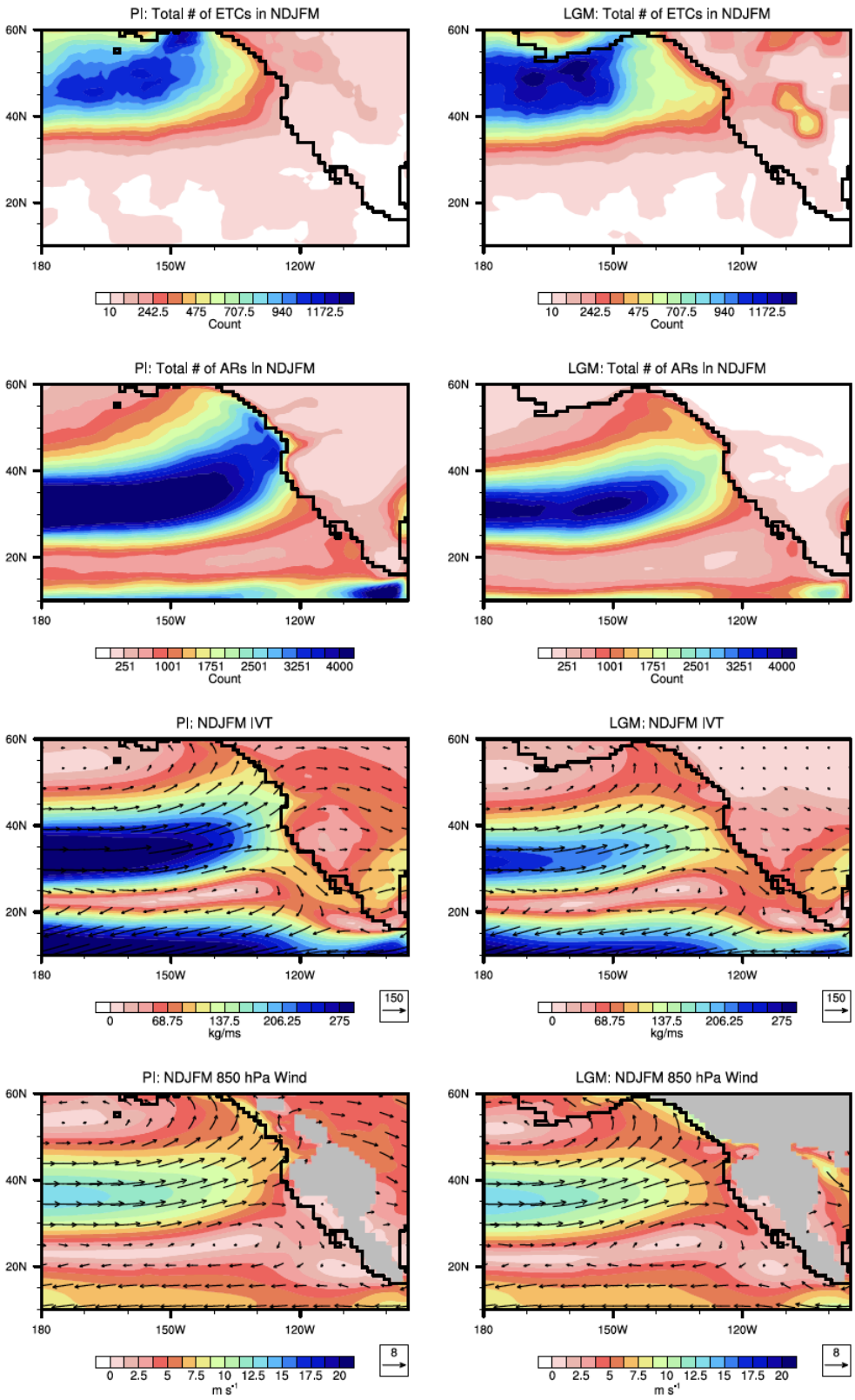

Figure S8: Same variables as Figure 5 but for PI (left column) and LGM (right column).

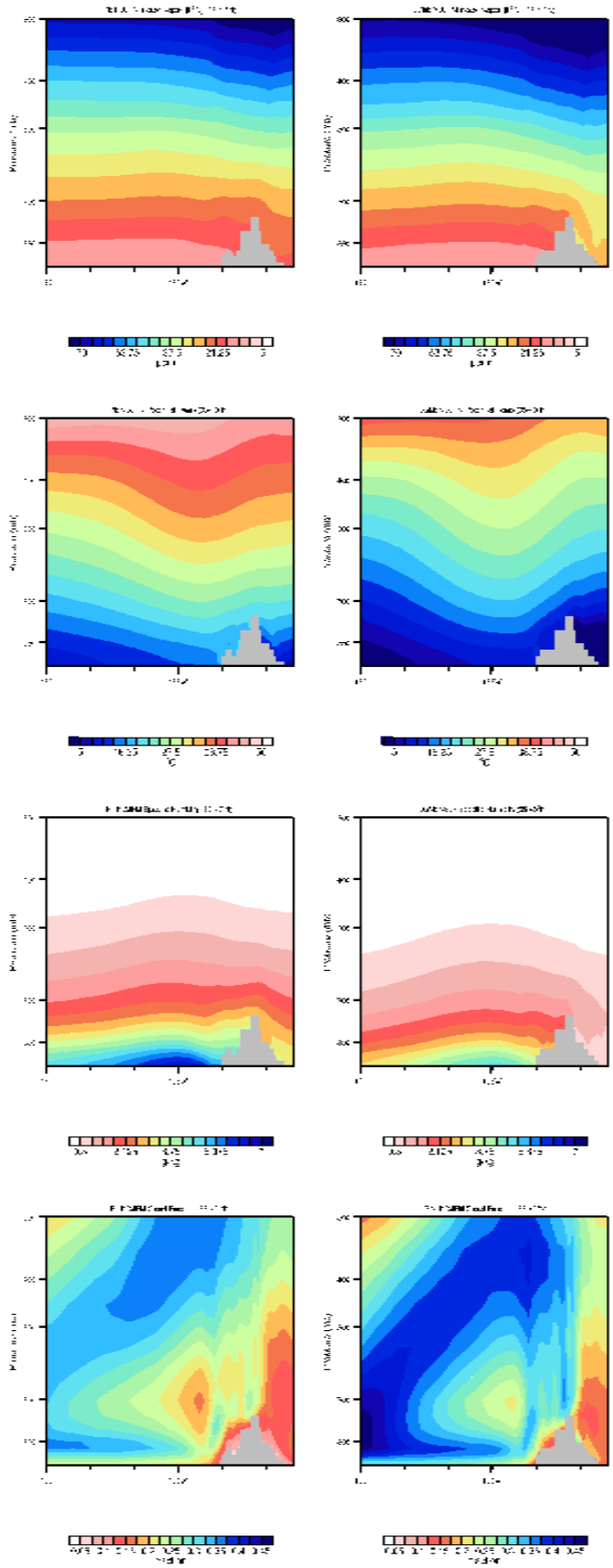

Figure S9: Same variables as Figure 6 but for PI (left column) and LGM (right column).

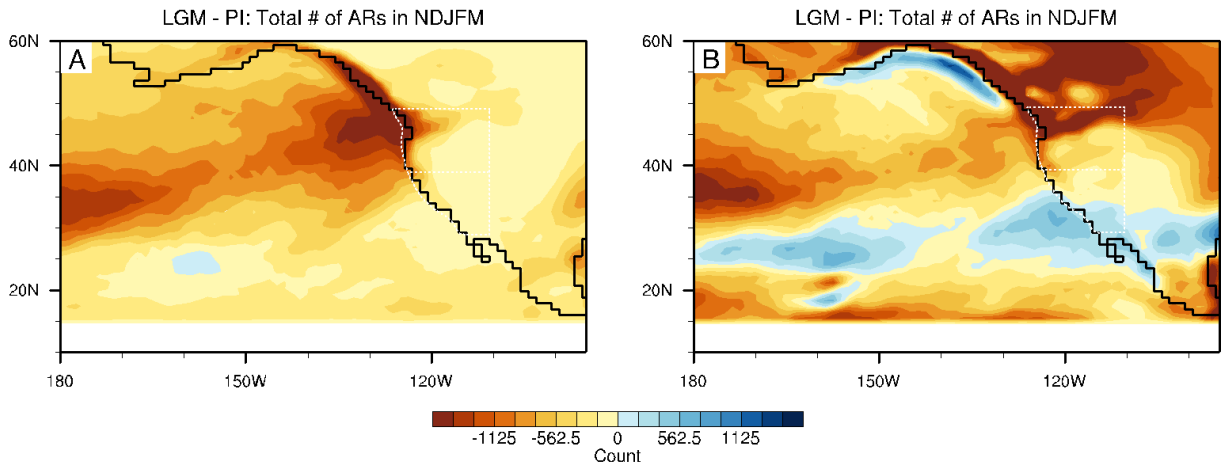

Figure S10: Comparing parameters for AR identification. A) Difference between winter LGM and PI AR frequency using 1) a minimum IVT threshold of 250 kg/m/s; 2) a minimum Laplacian of IVT of 50,000 kg/m/s/degrees^2; 3) a minimum IVT area of 5 grid cells; 4) a radius of the discrete Laplacian of 20 grid cells; and 5) a minimum latitude of 15°N. B) Difference between winter LGM and PI AR frequency using 1) a minimum IVT threshold of 125 kg/m/s; 2) a minimum Laplacian of IVT of 25,000 kg/m/s/degrees^2; 3) a minimum IVT area of 3 grid cells; 4) a radius of the discrete Laplacian of 10 grid cells; and 5) a minimum latitude of 15°N. This shows a regional increase in AR frequency at the LGM when using less restrictive thresholds, which agrees with the increase in North Pacific ETC frequency at the LGM. However, the less restrictive AR thresholds used in panel B) lead to a PI AR frequency beyond most common AR identification techniques. Northwest and Southwest United States regions outlined with dashed white lines. LGM continental configuration outlined in black.